Interactions of Tropopause Depressions with an Ex–Tropical Cyclone and Sensitivity of Forecasts to Analysis Errors

K. A. BROWNING, A. J. THORPE, A. MONTANI, D. PARSONS,* M. GRIFFITHS, P. PANAGI, AND E. M. DICKS

Joint Centre for Mesoscale Meteorology, Department of Meteorology, University of Reading, Reading, United Kingdom

(Manuscript received 23 February 1999, in final form 9 November 1999)

ABSTRACT

This paper focuses on the coupling between an ex–tropical cyclone and two preexisting mesoscale tropopause depressions (TDs). The TDs approached the cyclone from widely separated sources after becoming cut off from different upper-level troughs upstream. The first part of the paper combines Meteosat imagery with products from the limited-area version of the operational U.K. Meteorological Office Unified Model to reveal the 3D structure and evolution of the mesoscale features. Each TD was a potential vorticity (PV) maximum characterized by dry-intrusion air descending slantwise beneath an upper-level jet streak. Each TD generated its own cloud head and each is believed to have contributed to the deepening of the surface cyclone. Later parts of the paper identify errors in model forecasts and attribute them to analysis errors in the position of one of the TDs. Two methods are used to locate the analysis errors. Both are capable of being used in real time. The first is the identification via satellite imagery of an error in the model's water vapor analysis. The second method, using singular vectors calculated for the ECMWF model, involves the identification of sensitive regions where any analysis error would be expected to grow rapidly. The regions highlighted by these two methods were broadly collocated. The present case is unusual in that the most sensitive region was in the upper troposphere. Forecast reruns made with the Met Office and ECMWF models after modifying the upper-level PV in the analysis showed some limited improvements.

1. Introduction

There is a large body of literature describing the cyclogenesis that results from the coupling of upper-tropospheric features with low-level baroclinic zones (see the review by Uccellini 1990). Accurate prediction of cyclone development depends on the ability of operational numerical weather prediction (NWP) models to represent such coupling processes in detail. It is therefore necessary to ensure that the features are properly represented in the model analyses. This presents a problem over data-sparse ocean areas. Thus much thought is currently being given to 1) devising methods of using satellite imagery to identify and apply adjustments to the model analyses (Mansfield 1997; Carroll 1997; Demirtas and Thorpe 1999) and 2) establishing the feasibility of making extra observations targeted on the regions that are predicted to be sensitive to errors in the initial analysis (Snyder 1996; Joly et al. 1997; Montani et al. 1999). To underpin the development of such techniques it is desirable to obtain a better understanding of the three-dimensional structure of the interacting components of the cyclone system and to examine the relationship of these dynamical components to the predicted regions of sensitivity of forecasts to errors in the initial structure: these are the objectives of the paper.

This paper presents a diagnostic study of a developing cyclone and brings together three methodologies: satellite imagery interpretation as pursued by Weldon and Holmes (1991) and Bader et al. (1995); ''potential vorticity (PV) thinking'' and attribution applied to NWP model output as advocated by Hoskins et al. (1985), Fehlmann and Davies (1997), Thorpe (1997), and Griffiths et al. (2000); and singular-vector analysis as a means of identifying regions where the cyclone forecasts are particularly sensitive to errors in the initial state (Buizza and Montani 1999). We use output from operational runs of the nominally 60-km grid, limited-area version of the U.K. Meteorological Office Unified Model (Cullen 1993) and the imagery from the water vapor channel of Meteosat. For the singular vector analyses the T69 version of the European Centre for Medium-Range Weather Forecasts (ECMWF) model is used.

The event analyzed in this paper is an Atlantic cy-

* On leave from National Center for Atmospheric Research, Boulder, Colorado.

Corresponding author address: Prof. K. A. Browning, Department of Meteorology, University of Reading, Earley Gate, P.O. Box 243, RG6 6BB Reading, United Kingdom.
E-mail: K.A.Browning@reading.ac.uk

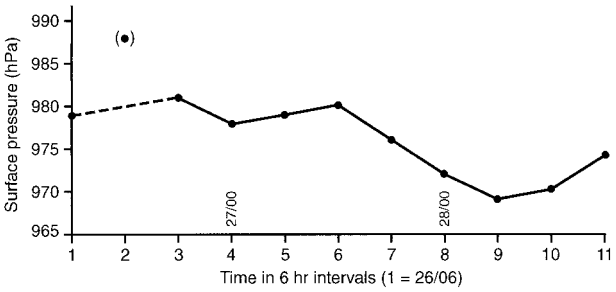

FIG. 1. Mean sea level pressure plotted at 6-h intervals from 0600 UTC 26 Oct 1996 (time code 1) until 1800 UTC 28 Oct. The bracketed value of MSLP at time code 2 is at the time of a badly bogused analysis and is thought to be grossly in error. The transition from a tropical to ex–tropical cyclone occurred at around time code 4.

clone in October 1996 that originated as Tropical Cyclone Lili. The cyclone was situated at 40°N, 36°W at 1200 UTC 26 October (26/12). A day later it was at 49°N, 20°W. By 28/12 it was over Ireland, centered at 53°N, 9°W. We study the cyclone just after its transition to an extratropical cyclone, which occurred at about 27/00. The broadscale evolution of the cyclone and its detailed mesoscale structure at the time of peak intensity have been analyzed by Browning et al. (1998). At peak intensity the cyclone produced severe gales and heavy rain over the British Isles and it still retained a warm core up to 400 hPa. Unified Model analyses and very short range ($T + 6$) forecasts verified well against continuous wind profiler measurements in Wales during the time of peak intensity. Here we shall be more concerned with the earlier reintensification period of the cyclone, centered at 28/00 (Fig. 1). For this period, when the cyclone was over the data-sparse ocean and the model performance was poorer (though still useful), we shall use Meteosat imagery as best we can to establish the model errors.

Mesoscale tropopause depressions associated with tropopause folds, hereafter referred to simply as tropopause depressions or TDs, played a key role in the reintensification process. There were two dominant TDs. One (TD1) originated as a cutoff from a large-scale trough to the west of the cyclone: see the small shaded area at 26/06 centered at 41°N, 53°W in Fig. 2a. The cyclone was still a tropical cyclone at this time. TD1 moved in a generally eastward direction [see sequence of PV charts in Fig. 5 of Browning et al. (1998)]. Twenty-four hours later it was situated just behind the cyclone at 46°N and 36°W (Fig. 2b). By now the cyclone had made the transition from tropical to extratropical. Subsequently another tropopause depression, TD2, became cutoff from the large-scale trough to the north of the cyclone and it then followed behind TD1 as they both interacted with the cyclone, skirting around its southern flank (Figs. 2c and 2d). This paper is about these interactions.

In section 2 we present a description of the cyclone structure during its reintensification phase. Key features of the structure are identified from model analyses and satellite imagery. Then in section 3 we focus on the evolution of individual TDs before and during their interaction with the cyclone. The model analyses reproduced the broad features quite well and are used without adjustment to describe the structure and evolution of the TDs in sections 2 and 3. Errors in the model analyses were, however, large enough to affect significantly the accuracy of the forecasts.

In section 4 we describe the forecast errors for the 24-h forecast that embraced the period of cyclone reintensification. This is done for the Unified Model forecast. We then look at the corresponding ECMWF forecast run and use the *known* forecast errors (i.e., known after the event) to estimate the analysis errors applicable at the start of that particular forecast run. This is done by projecting the known errors in the ECMWF forecast onto the dominant singular vectors and then using the so-called pseudoinverse method (Montani 1998). We also show the results of an ECMWF forecast rerun with these errors removed to confirm that the diagnosed analysis error is indeed sensible.

We then address the question, in section 5, as to whether we could have estimated the analysis error using *only information available at analysis time.* First we use water vapor (WV) imagery to estimate analysis errors in the upper-level PV field. Then we look at the singular vector analysis to identify the region to which the forecast was most sensitive to analysis errors. The location of this so-called sensitive region is shown to coincide with the main region of analysis error identified from the imagery.

Finally, in section 6, we use the PV modification technique in the form described by Griffiths et al. (2000) to apply the adjustment determined from the WV imagery to see if the resulting reanalysis gives rise to an improved forecast. Although the impact is small, we argue that there is some potential in the PV–WV approach, at least in those cases where the analysis error is predominantly at upper levels. In some future operational scenarios it may be possible to supplement this approach with data from targeted unmanned aircraft directed to regions identified either from the singular vectors or the WV imagery.

2. Analysis of the structure of the cyclone during its reintensification phase

a. Conceptual model of cyclone structure during coupling with a single tropopause depression

To assist in the interpretation of the more complex real data that follows, Fig. 3 shows some general features of the structure of a cyclone during coupling with a *single* tropopause depression. This figure is based on the idealized model in Fig. 1 of Browning et al. (1995) but it bas been adapted in order to relate better to the case analyzed in the present paper. (The main differ-

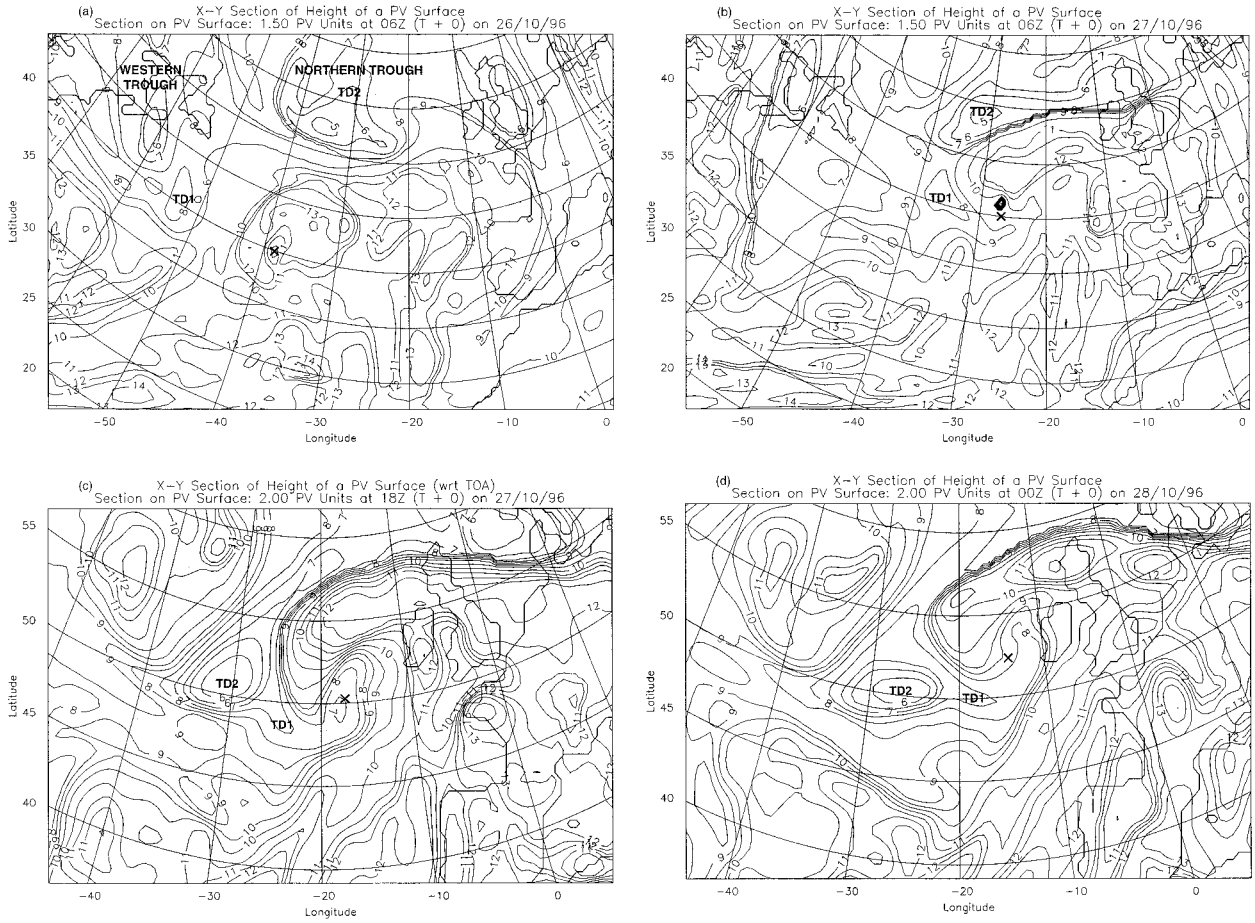

FIG. 2. Tropopause height (in km), as derived from the Met Office Limited Area Model analyses for (a) 0600 UTC 26 Oct, (b) 0600 UTC 27 Oct, (c) 1800 UTC 27 Oct, and (d) 0000 UTC 28 Oct 1996. The PV threshold used to represent the tropopause is changed from 1.5 to 2 PV units halfway through this sequence in order to achieve better discrimination of wanted features. Here, (c) and (d) cover the same reduced area as most of the later diagrams; however, (a) and (b) cover a larger area in order to show the origins of the two TDs. Large shaded areas in (a) and (b), with tropopause height less than 8 km, draw attention to major upper-level troughs to the west and north of Tropical Cyclone Lili, the MSL pressure center of which is denoted by X. The transition of Lili from a tropical to an extratropical cyclone occurred about 6 h before (b). The small shaded area, centered 15° west of the cyclone in (a) and 10° west of the cyclone in (b), is the mesoscale tropopause depression referred to as TD1, which has broken away from the western trough. Subsequently another mesoscale tropopause depression (TD2) broke away, this time from the northern trough, and (c) and (d) show it approaching the cyclone behind TD1.

ence is that in the previous model the flows were more elongated in the front-parallel direction owing to the stronger stretching deformation in that case. Also the orientation of the pattern has been rotated cyclonically to correspond to the rather nonstandard orientation of the pattern in the present case). The model in Fig. 3 consists of two interlocking flows: a dry-intrusion flow (Browning 1997) and a moist high-θ_w flow (θ_w is wet-bulb potential temperature). To a first approximation these flows are mirror images of each other in the vertical, but laterally displaced. The ascent of the high-θ_w flow is responsible for the upper parts of a cloud head (Böttger et al. 1975; Browning and Roberts 1994a), whose top rises toward a characteristically curved convex outer boundary CC. The area of descending dry-intrusion air extends down from the region of the tropopause depression. As shown in the cross section XX′, the stratospheric part of the dry intrusion descends beneath a jet streak as a tropopause fold into the middle and lower troposphere. Nearby tropospheric air also descends and gives rise to an extension of the dry intrusion, which reaches down to the top of the boundary layer close to the associated cold front. This conforms to the model of Danielsen (1964) (reproduced in Fig. 1 of Browning 1997). Whereas the frontal structure in the vicinity of WW′ corresponds to that of an anafront, that near XX′ corresponds to a katafront characterized by less high cloud and often not much precipitation.

A close examination of the case in the present paper shows that although it conforms broadly to Fig. 3, it is more complicated in that there were two sets of partially overlapping structures of this kind. Actually there were more than two (identified by numbers 0, 1, and 2) but

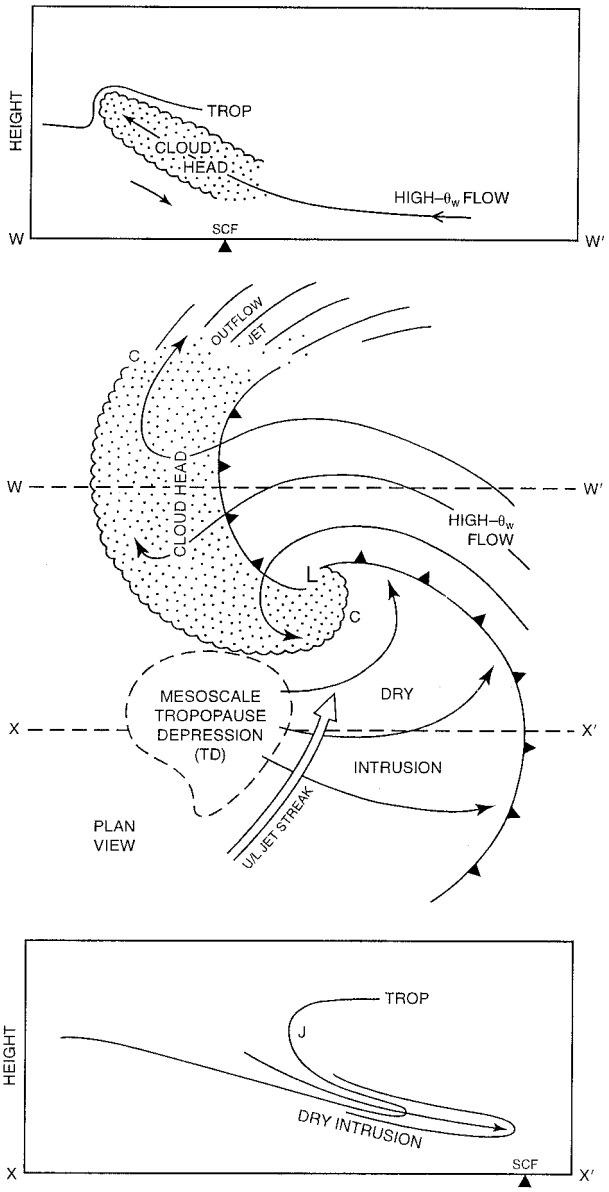

FIG. 3. Idealized model showing the intertwining around a cyclone center (L) of two rather symmetrical flows: the dry-intrusion flow descending from the mesoscale tropopause depression (low wet-bulb potential temperature, θ_w) and the flow of high-θ_w air ascending into the cloud head. Middle part of figure is a plan view; upper and lower panels show vertical sections along WW′ and XX′, respectively. The black triangles in these sections denote the positions of the surface cold fronts (SCFs). The cold front bounding the cloud head corresponds to what is often analyzed as a bent-back warm front but which is in fact traveling toward the warm air. An upper-level jet streak occurs at the leading edge of the mesoscale tropopause depression and the outflow from the cloud head feeds an upper-level outflow jet.

our analyses will concentrate on the two major ones associated with the two tropopause depressions, TD1 and TD2. We show that each of these was associated with its own PV streamer (S1 and S2), dry intrusion (D1 and D2), cold front (CF1 and CF2), upper-level jet streak (J1 and J2), and cloud head (CH1 and CH2). This duality obviously complicates the interpretation but is something that occurs often and has to be taken into account in practical forecasting situations. Double structure of this kind was, for example, a feature of the FRONTS-92 cyclone analyzed by Browning et al. (1995, 1997) but the duality in the present case was more pronounced and more easily resolved. In cases such as this the questions arise as to which, if any, tropopause depression is going to interact with a cyclone and with what consequences. We address these questions in sections 4 and 5.

b. Synoptic overview based on the NWP model analysis for 0000 UTC 28 October

Figure 4 provides an overview of the cyclone structure at 28/00 when the cyclone was deepening rapidly during its extropical phase. Figure 4a shows the surface low west of Ireland with a central pressure of 972 hPa and two cold fronts, one over England and Wales, and the other approaching Ireland. These fronts, CF1 and CF2, were associated with other similarly numbered features (TD1/TD2, S1/S2, J1/J2, CH1/CH2) discussed later in this section. The cold fronts are evident in the θ_w pattern at 800 hPa (Fig. 4b) and they could also be discerned in the infrared satellite imagery (not shown) when suitably enhanced to reveal the small differences between the temperatures of the sea surface and the tops of boundary layer clouds: the passage of CF1 coincided with a clearance in the cloud while the passage of CF2 heralded the onset of shallow boundary layer convection. The warm core of the cyclone is also evident in Fig. 4b; the warmest part of the seclusion has a θ_w exceeding 291 K.

Figure 4c shows that the high-θ_w flows at low levels just ahead of each cold front were characterized by higher relative humidity, and these flows fed into a generally saturated region corresponding to the main cloud head. As discussed later, much of the cloud head (CH1) at this time was associated with TD1; however, tropopause depression TD2 was beginning to have an effect at this time, with a new cloud head (CH2) beginning to develop behind CH1. TD2 had a major effect on the cyclone development, which is perhaps not surprising in view of the magnitude of its potential vorticity: Fig. 4d shows a peak value of almost 4 PV units at 400 hPa (centered at 50°N, 27°W). Smaller PV maxima, of 1.4 PV units at this pressure level, can be seen located ahead of TD2, (centered at 50°N, 18°W and 51°N, 12°W) in association with TD1 and TD0, respectively. These were circulating around the cyclone's warm core and its diabatically generated PV maximum, the 700-hPa extent of which is shown in Fig. 4e. Later (section 3) we shall examine the evolution of the PV maxima associated with TD1 and TD2. The best continuity was achieved by tracking them at 300 hPa.

Further insight into the 3D structure of the cyclone

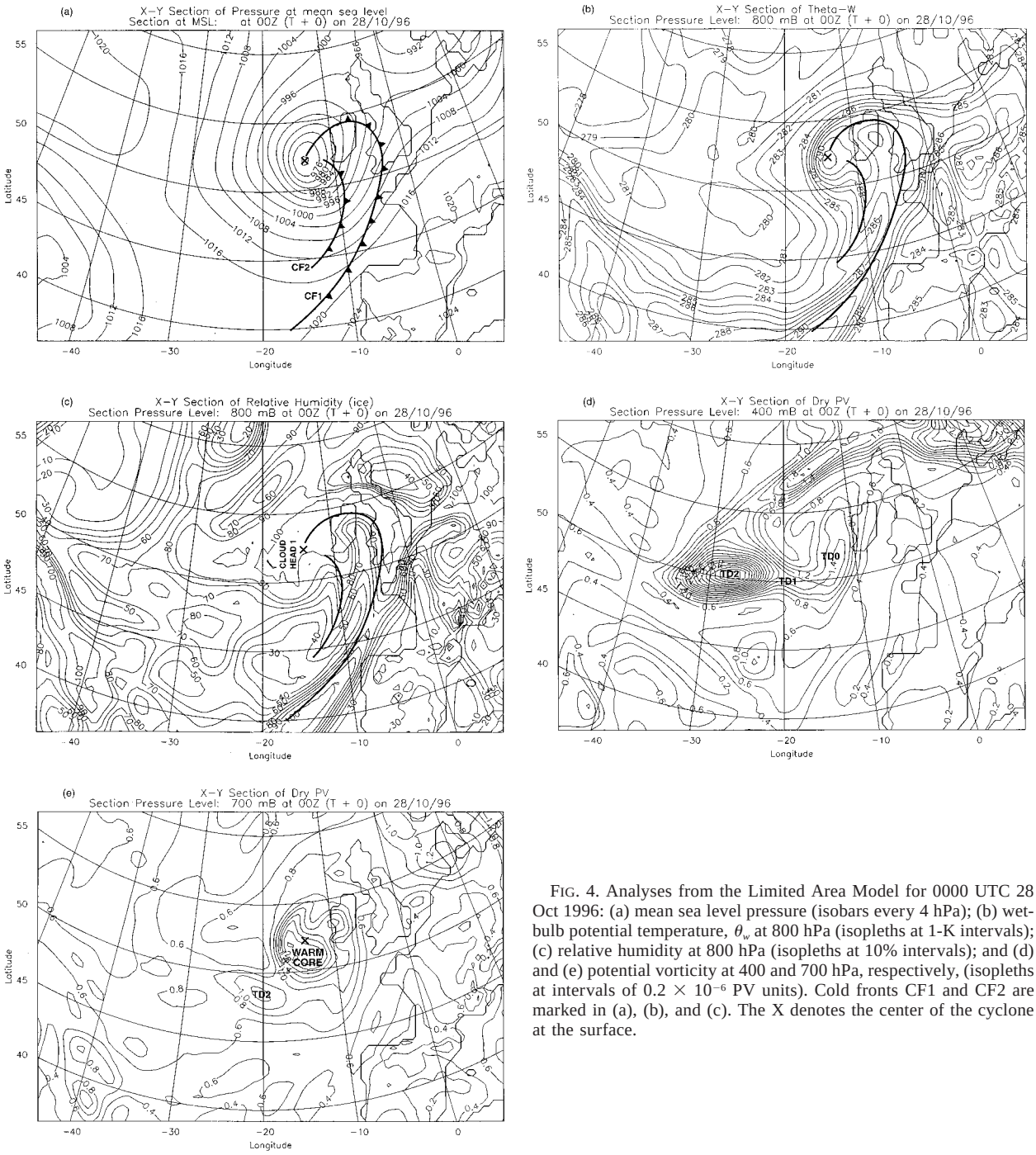

FIG. 4. Analyses from the Limited Area Model for 0000 UTC 28 Oct 1996: (a) mean sea level pressure (isobars every 4 hPa); (b) wet-bulb potential temperature, θ_w at 800 hPa (isopleths at 1-K intervals); (c) relative humidity at 800 hPa (isopleths at 10% intervals); and (d) and (e) potential vorticity at 400 and 700 hPa, respectively, (isopleths at intervals of 0.2×10^{-6} PV units). Cold fronts CF1 and CF2 are marked in (a), (b), and (c). The X denotes the center of the cyclone at the surface.

can be gained by examining the structure within a sloping isentropic surface. This is pursued later, in section 2d, with particular reference to the dry intrusions associated with the tropopause depressions. Before presenting the isentropic analyses, however, it is helpful to establish the validity of the cloud-head and dry-intrusion features as entities from their appearance in the satellite imagery.

c. Cloud heads and dry intrusions as seen in satellite imagery

1) CLOUD HEADS

Cloud heads are best seen in infrared imagery and dry intrusions, or at least their upper parts, are best seen in water vapor imagery. Since there is also a good signature of cloud heads in water vapor imagery, we shall

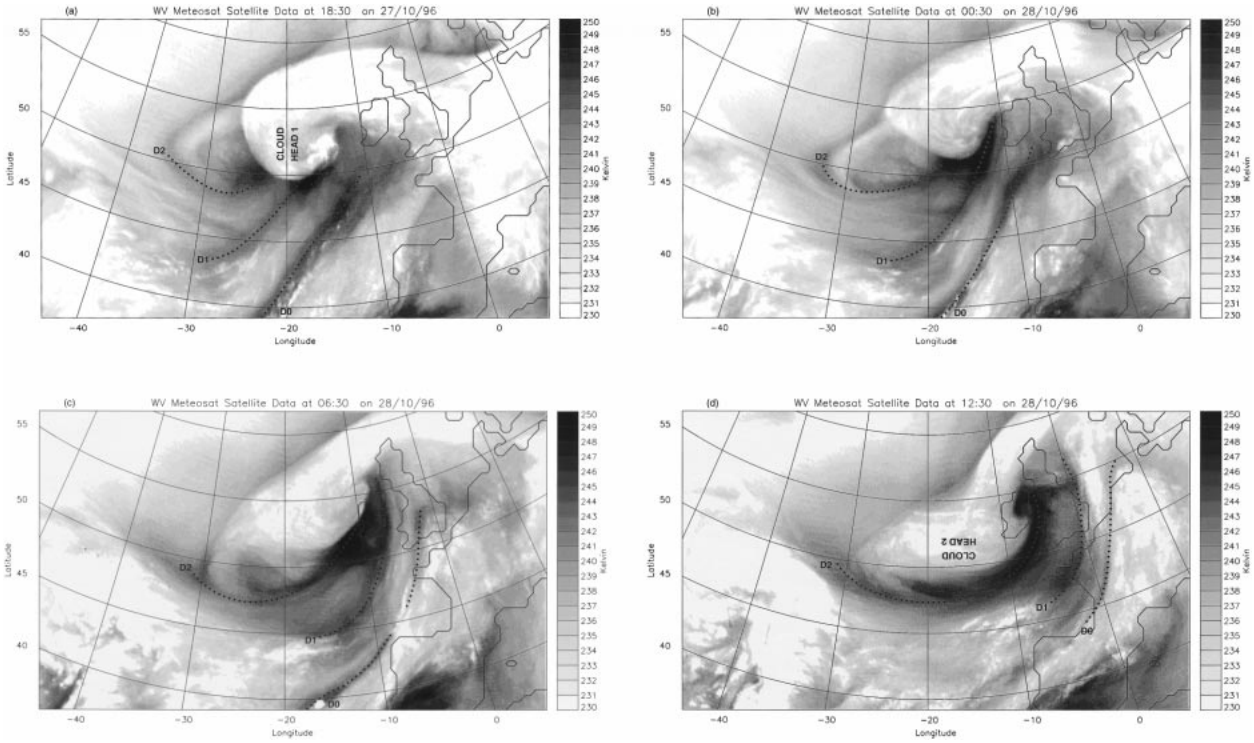

FIG. 5. Meteosat water vapor images showing the distribution of upper-tropospheric water vapor (and cloud) associated with the cyclone at (a) 1830 UTC 27 Oct, and (b) 0030, (c) 0630, and (d) 1230 UTC 28 Oct 1996. The dotted lines draw attention to the axes of three dark zones corresponding to the upper parts of dry intrusions D0, D1, and D2.

restrict ourselves here to showing the latter. Figures 5a–d show the Meteosat water vapor imagery at 6-h intervals from 27/1830 to 28/1230 during and just after the period of cyclone reintensification. During this period there were two cloud heads in succession, CH1 and CH2.

At 27/18 (Fig. 5a) cloud head 1 is the westernmost part of the smoothly curved extension of a band of cloud trailing westward from the British Isles. The cyclone center is at the southeastern tip of the cloud head (50.5°N, 18°W). The orientation of this cloud head corresponds to that in the conceptual model in Fig. 3: the NWP model shows that warm moist boundary layer air ascends within it with a component from right to left toward the convex outer boundary CC. Figures 5b and 5c show CH1 traveling northeastward: during this period a new cloud head (CH2) develops close by to the south and merges with it. By 28/12, Fig. 5d shows that CH1 has been replaced by the new cloud head CH2 with its convex outer boundary CC orientated east–west along 50°N. To conform with the labeling convention adopted in Figs. 3 and 5a (in which the label is the right way up when viewed traveling with the high-θ_w flow into the cloud head), CH2 is labeled upside down in Fig. 5d. The cyclone center is over Ireland at this time, close to the northward-directed hook of cloud at the eastern end of the cloud head. High-θ_w air entering this cloud head was now rising slantwise from north to south and fanning out toward the reorientated boundary CC. In the hooked part of the cloud head over Ireland this air flow curves cyclonically first toward the east and then north. As shown by Browning et al. (1998) this was a region of heavy rain with severe gales on its flank.

2) MULTIPLE DRY INTRUSIONS

The water vapor images in Figs. 5a–d show dark zones surrounding the cloud head. Such dark zones show the location of dry air in the upper and middle troposphere (Weldon and Holmes 1991). The axes of these dark zones, identified by dotted lines, are associated with dry intrusions labeled D0, D1, and D2. Examination of this sequence of images reveals how these dry intrusions were being advected cyclonically around the cyclone center. The dark zones D1 and D2 are due to the two main dry intrusions, which we later show to be related to tropopause depressions TD1 and TD2, and to cloud heads CH1 and CH2. The rather light gray hook-shaped feature in Figs. 5a–c just north of the axis of D2 and projecting from the cloud head CH1 southwestward toward the label D2 is the incipient cloud head associated with TD2. It circulated around the southwestern boundary of CH1 and (part of it) developed into cloud head CH2, shown in Fig. 5d. In section 5a, we compare in detail the positions of these features in the imagery with corresponding features in the model:

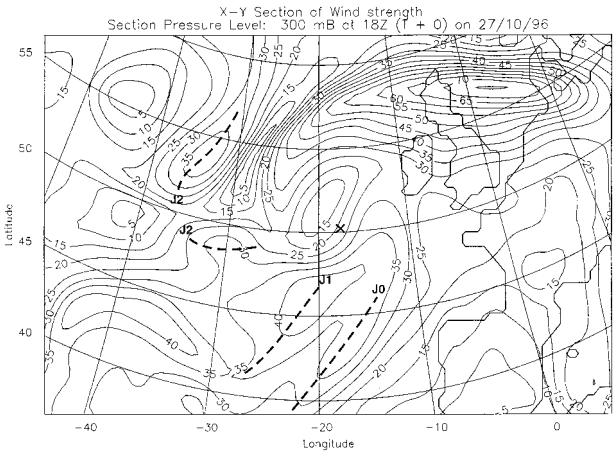

FIG. 6. Wind strength (in m s^{-1}) at 300 hPa, as derived from the Limited Area Model analysis for 1800 UTC 27 Oct 1996. The dashed lines draw attention to jet streaks J0, J1, and J2 (there are two parts to J2 as explained in the text: the southern part intensifies at the expense of the northern part during the next 12 h). The X marks the location of the surface cyclone center.

this provides confidence in the model's ability to represent such features at all, while at the same time quantifying errors in the precise position of one of these features in the model.

Between each of the dark zones (dry intrusions) identified in Fig. 5, there are lighter gray wedges of moist air, possibly with small remnants of dissipating cirrus in some of them. These correspond to the warm moist wedges of Weldon and Holmes (1991). Weldon and Holmes draw attention to the fact that the edges of the moist wedges on the flank of the cyclone correspond to jet streaks. The same relationship applies in the present case, as shown by the model-derived 300-hPa wind speeds depicted in Fig. 6. The jet streaks J0, J1, and J2 in Fig. 6 are seen to be located just in advance of the corresponding dry-intrusion axes, D0, D1, and D2 in Fig. 5a. Although the dark zones show up in the imagery as relatively narrow axes of dry air aloft, we shall show in section 3d that the associated dry intrusions were extensive sloping layers that undercut the moist air in the jet streaks (the moist wedges) as the dry-intrusion air descended toward the boundary layer. [A complication revealed by Fig. 6 is that J2 was in two parts at 27/18. As we shall show in section 4, TD2 was just beginning to interact with the cyclone and its leading edge was beginning to extend around the southern flank of the cyclone. Curvature effects alone could account for the gap in the isotach pattern associated with J2 at this time. Six hours earlier there had been no sign of the leading part of J2, and even at the time of Fig. 6 it is still not well defined. However, 6 (12) h later, the leading part of J2 elongated and increased in speed to over 35 (45) m s^{-1}, while the speed of the original, trailing part of J2 had decreased to 30 (25) m s^{-1}.]

d. The three-dimensional structure of the dry intrusions as given by NWP model isentropic analysis

According to Fig. 4, cold front CF2 was situated well ahead of its associated tropopause depression TD2 (the former was close to 10°W and the latter was centered at 27°W). We now show a series of model analyses for 28/00 (Fig. 7) that show that these two features were connected by a dry-intrusion flow that descended slantwise ahead of TD2 and interacted with the cyclone itself. The dominant feature in the cross section in Fig. 7a is the long (dark gray) finger of dry air associated with dry intrusion D2, which is characterized by air with relative humidity less than 10% down to 700 hPa. Figure 7a shows that D2 (the lower part of which was centered on the 305-K isentrope) was associated with a PV streamer (itself centered on the 300-K isentrope) with values of 1 PV unit also coming down to 700 hPa. Similar fingers of dry-intrusion air are evident in parallel sections (not shown) on either side of that in Fig. 7a, showing that they were parts of broad curtains of air that descended toward the cold front as shown schematically in Fig. 3, and discussed by Danielsen (1964) and Young et al. (1987).

The details of this descent are depicted in the isentropic analysis for the 305-K θ_w surface, shown in Figs. 7b–e. Figure 7b gives the topography of the surface. It is highest (6.4 km) near the center of the tropopause depression (which according to Fig. 7c has a maximum PV of 2.8 PV units in this surface) and lowest (2.4 km) in the warm core of the cyclone (which according to Fig. 7c has a maximum PV of 2.2 PV units in this surface). The flow in this surface relative to the cyclone's movement (11 m s^{-1} from 230°) is shown in Fig. 7d to be from west to east down the isentropic surface from the southern side of TD2 toward the surface cold front, near which the flow turns northward just ahead of the cyclone. The resulting dryness of this flow (D2) is shown in Fig. 7e. Although this dry intrusion was responsible for one of the dark zones shown in the WV imagery (Fig. 5b), much of it was obscured by overlying moist air and only its westernmost parts were visible in the imagery. This is an important limitation that must be kept in mind when relating imagery and model products.

Dry intrusion D2 was behind dry intrusion D1, and also D0, and it was undercutting both of them at this time. The sections farther north (not shown) depict D1 and D0 more clearly, but vestiges of them can nevertheless be seen in Fig. 7a as short (dark gray) dry fingers between 400 and 500 hPa at ranges between 1300 and 2000 km. The upper parts of D1, as well as D0, are partly obscured from satellite view by moist air overunning them near 300 hPa, associated with jet streaks J1 and J2, as labeled in Fig. 7a. These moist patches correspond to the ''moist wedges'' referred to earlier in connection with the WV imagery in Fig. 5.

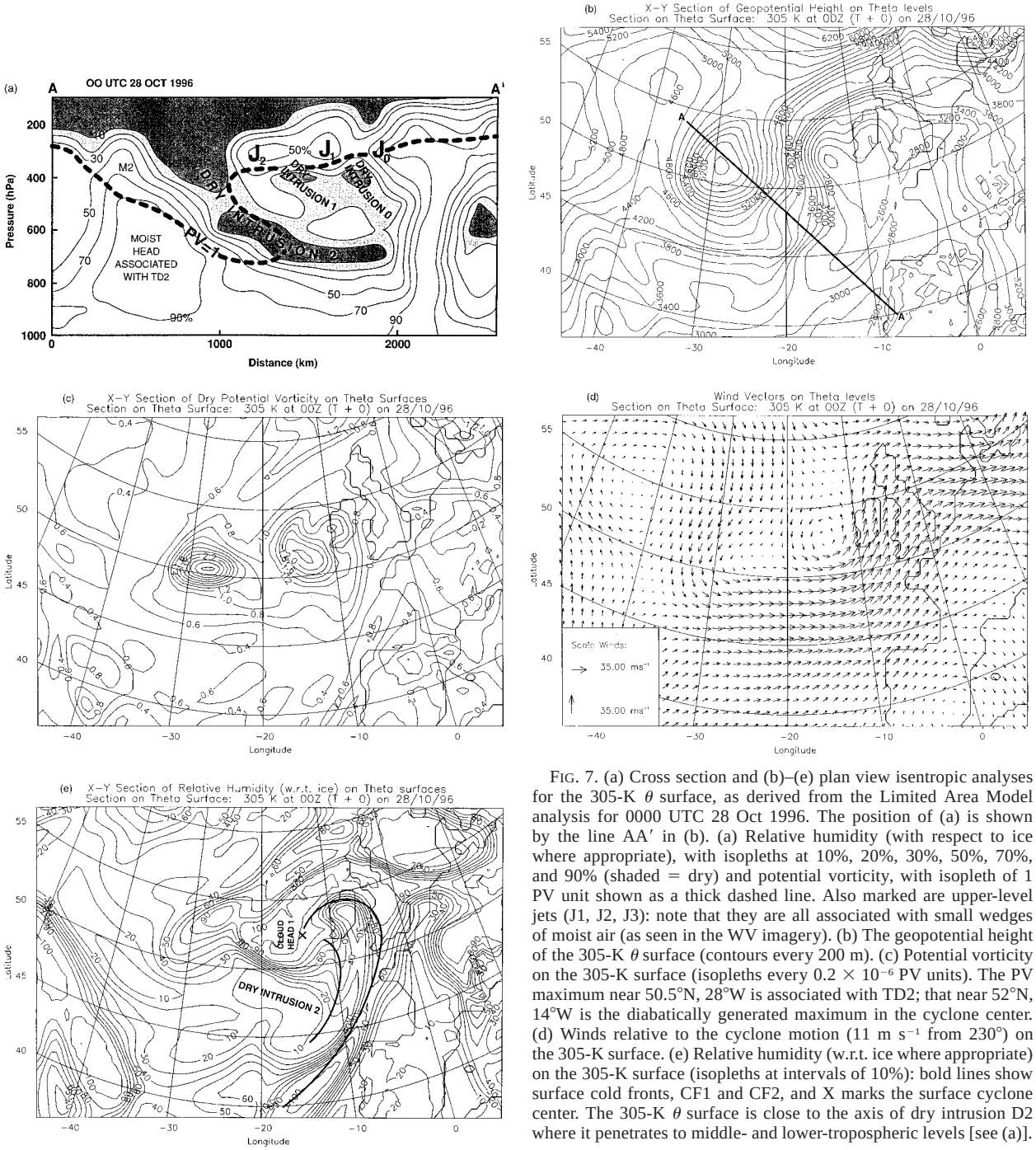

FIG. 7. (a) Cross section and (b)–(e) plan view isentropic analyses for the 305-K θ surface, as derived from the Limited Area Model analysis for 0000 UTC 28 Oct 1996. The position of (a) is shown by the line AA′ in (b). (a) Relative humidity (with respect to ice where appropriate), with isopleths at 10%, 20%, 30%, 50%, 70%, and 90% (shaded = dry) and potential vorticity, with isopleth of 1 PV unit shown as a thick dashed line. Also marked are upper-level jets (J1, J2, J3): note that they are all associated with small wedges of moist air (as seen in the WV imagery). (b) The geopotential height of the 305-K θ surface (contours every 200 m). (c) Potential vorticity on the 305-K surface (isopleths every 0.2×10^{-6} PV units). The PV maximum near 50.5°N, 28°W is associated with TD2; that near 52°N, 14°W is the diabatically generated maximum in the cyclone center. (d) Winds relative to the cyclone motion (11 m s^{-1} from 230°) on the 305-K surface. (e) Relative humidity (w.r.t. ice where appropriate) on the 305-K surface (isopleths at intervals of 10%): bold lines show surface cold fronts, CF1 and CF2, and X marks the surface cyclone center. The 305-K θ surface is close to the axis of dry intrusion D2 where it penetrates to middle- and lower-tropospheric levels [see (a)].

3. Evolution of the mesoscale tropopause depressions and their interaction with the cyclone

Local upper-level maxima in PV associated with tropopause depressions TD1 and TD2 were discernable in successive model analyses. In this section we shall analyze the evolution of these PV maxima as a way of determining the interactions of the TDs with the cyclone. The upper-level PV maxima were tracked on isentropic surfaces, on isobaric surfaces, and in terms of the height of the constant-PV surfaces as in Fig. 2. We have chosen to present the tracks of PV in the 300-hPa isobaric surface because this gave the longest period of trackability. Isobaric tracking suffers from lack of conservation of PV and provides no quantitative measure of the vertical motion of the PV anomalies. Nevertheless

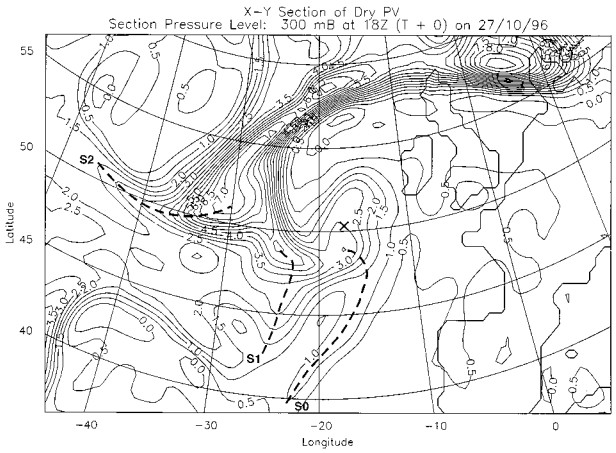

FIG. 8. Potential vorticity (isopleths at intervals of 0.5 PV units) at 300 hPa, as derived from the Limited Area Model analysis for 1800 UTC 27 Oct 1996. The dashed lines draw attention to PV streamers S0, S1, and S2. These streamers are the upper-level manifestation of sheetlike PV maxima that extend downward slantwise toward the south and east. Note the correspondence between the axes S0, S1, S2 and those of D0, D1, D2, and J0, J1, J2 in Fig. 5 (and Fig. 15) and Fig. 6, respectively. The X marks the surface cyclone center.

one is able to use increases in PV at 300 hPa qualitatively to infer descent of a PV anomaly. The resulting inferences are consistent with the trends in height evident in Fig. 2.

We shall analyze the temporal changes shortly but first we show a snapshot of the 300-hPa pattern of PV at 27/18 (Fig. 8), at a time that corresponds to the satellite WV image in Fig. 5a. Figure 8 shows that the model resolved three 300-hPa PV maxima corresponding to TDs 0, 1, and 2 as they encircled the cyclone: TDs 0, 1, and 2, respectively, display closed contours of 3.5, 5, and 7 PV units at this level. Each PV maximum was a dry feature, distinct from the column of diabatically generated PV situated at lower levels within the cyclone. And each PV maximum is seen in Fig. 8 to be located at the end (closest to the cyclone) of PV streamers, labeled S0, S1, and S2, which radiate outward from the cyclone center and correspond to the dark zones seen in the WV imagery. Specifically these streamers are associated with corresponding dry intrusions (D0, D1, D2) and jet streaks (J0, J1, J2) depicted in Figs. 5a and 6, respectively. Plan sections at lower levels (not shown) demonstrate that the PV streamers are sections through curtains (layers) of maximum PV that slope downward toward the south and east in the same manner as the dry intrusions.

The evolution of the 300-hPa PV maxima in relation to the cyclone is shown in Fig. 9. The figure is in four parts. The first part (Fig. 9a) shows the tracks of the 300-hPa PV maxima corresponding to TD1 and TD2, and of the cyclone center, *relative to the earth*; the Figs. 9b and 9c respectively, show the tracks of TD1 and TD2 *relative to the cyclone center,* with the model's cloud head and coastlines shown for the time 27/18. The two TDs could be tracked unambiguously through 11 successive 6-hourly model analyses. As noted earlier in connection with Fig. 2 they came from different large-scale troughs: TD1 from the western trough and TD2 from the northern trough. In each case the track of the TD in the model began to deviate once the center of the TD came within 700 km of the cyclone center, at which stage the leading edge of its PV anomaly would have been approximately above the outer boundary of the cyclone's warm core. Thereafter each TD adopted a track that took it cyclonically around the southern boundary of the warm core.

Figure 9b shows that the track of TD1 began to change direction at 27/06 (time code 5). It then skirted around the cyclone until 28/18 (time code 11). Figure 9d shows that the peak value of PV at 300 hPa was between 2.5 and 3.5 PV units until 27/12. It then increased to (and thereafter remained) between 5 and 5.5 PV units presumably as a result of descent accompanying the interaction with the cyclone's warm core.

Figure 9c shows that tropopause depression TD2 began to deviate at 27/18 (time code 7). (The apparent growth in the area of TD2 at this time is illusory: as explained in the figure legend, different PV contours are used at different times and a lower-valued PV contour was used at this time.) This deviation happened as TD2 became elongated, with a new PV core developing at 300 hPa, 300 km ahead of the original TD2 core (see dumbbell shape of PV at time 7). Figure 9c shows that the new core associated with TD2 was an offshoot from the original TD2 core and its development at the expense of the original core appears to have been due to differential vertical motion in its vicinity. The newly descending PV core at this time was associated with the development of the new (leading) part of jet streak J2 as discussed earlier in section 2c. The relationship between the elongation of PV centers in troughs and PV gradients, jet streaks, and upper-level fronts is discussed in Davies and Rossa (1998) and references therein. Figure 9c shows that the new part of TD2 encircled the cyclone from 27/18 until (and beyond) 28/18 (time code 11). Figure 9d shows that TD2 was characterized by a large 300-hPa PV of 6 units from the very beginning. It then fluctuated between 6 and 8.5 units, before stabilizing at close to 7.5 units as it skirted the cyclone; that is, it did not strengthen significantly while interacting with the cyclone's warm core. At lower levels, at 27/18, TD2 was pulled out into a filament (fold) (cf. Fig. 7a), which was centered on the 305-K isentrope. When tracked in this surface the leading edge of the filament (at PV = 1.2 PV units) descended from about 4.5 to 3.5 km between 27/06 and 28/00 (time codes 5–8) where it remained for the next 18 h.

The behavior of the two main mesoscale tropopause depressions may be summarized as follows.

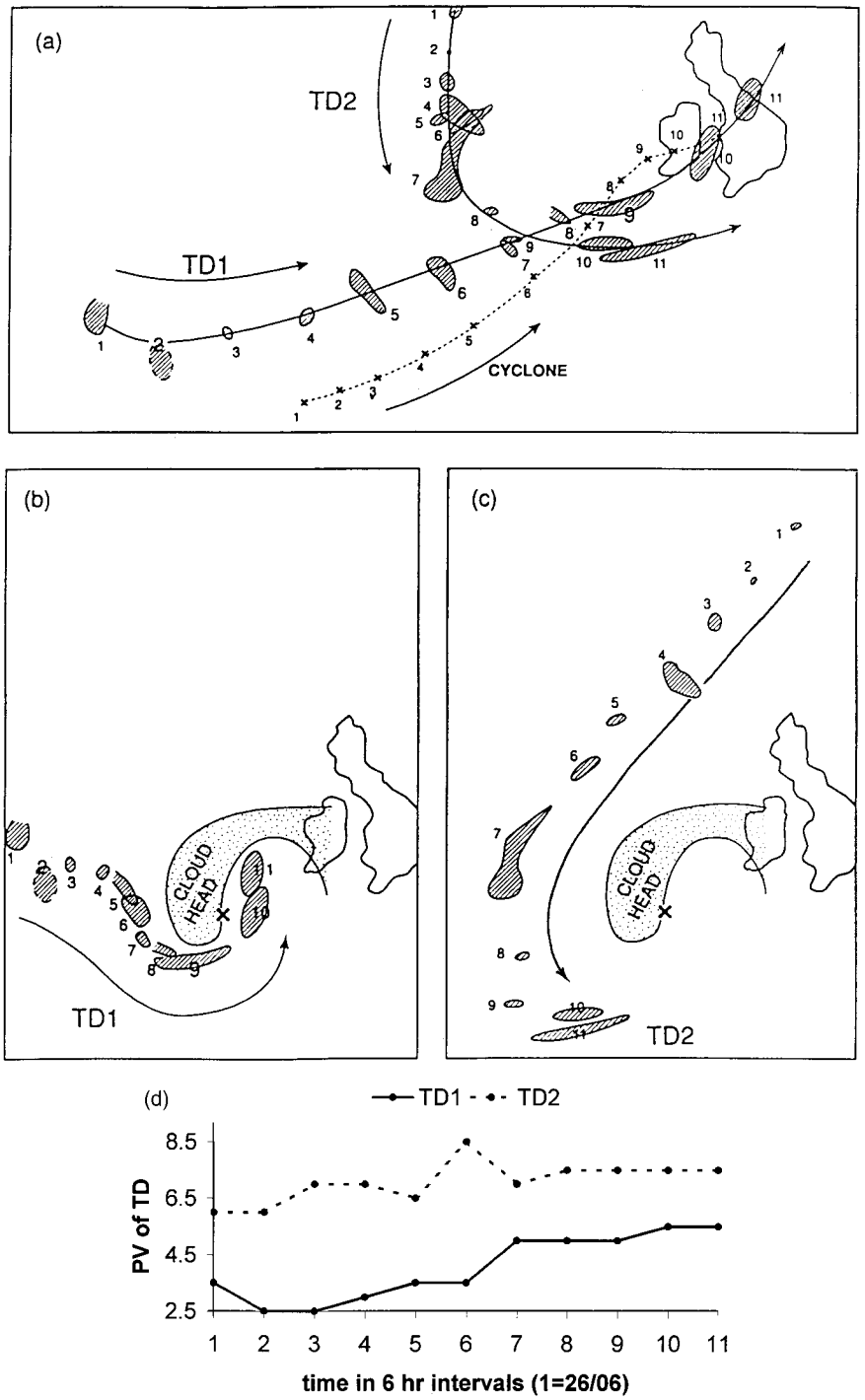

FIG. 9. Tracks and intensity of mesoscale tropopause depressions TD1 and TD2 in relation to the cyclone center as represented by their 300-hPa potential vorticity cores at 6-h intervals derived from the Limited Area Model analyses between 0600 UTC 26 Oct and 1800 UTC 28 Oct 1996. The time code used is in 6-h steps with 1 corresponding to 26/06 and 11 corresponding to 28/18. (a) Tracks of TD1 and TD2 relative to the earth; also shown is the track of the cyclone center (dotted line connecting crosses). Tracks of (b) TD1 and (c) TD2 relative to the surface cyclone center. The positions of the cloud head (given here by the model's upper-level relative humidity $>$ 75%), the British Isles coastline, and the cyclone center at 1800 UTC 27 Oct are drawn in (b) and (c) for reference. The PV contours in (a), (b), and (c) are the highest integral-valued contours at each time. (d) The peak value of the 300-hPa PV of TD1 and TD2 over the period depicted in (a), (b), and (c).

1) The two TDs were cut off from two separate troughs upwind of the cyclone.
2) Both began to deviate perceptably in their motion when they came close to the edge of the cyclone's warm core. We hypothesize that this deviation is an indication that the TDs were beginning to couple with the cyclone.
3) After coupling, they skirted around the southern flank of its warm core: TD2 followed behind TD1.
4) TD1 had a peak value of about 3 PV units at 300 hPa before coupling but this increased to about 5 units following coupling, implying substantial descent. TD2 retained a value of about 7 units throughout.
5) The increase in the 300-hPa PV of TD1, which took place between 27/12 and 27/18 (Fig. 9d), occurred at the same time that the mean sea level (MSL) pressure of the cyclone began to decrease (Fig. 1).

A diagramatic summary is given in Table 1 to clarify the timing of the above events and their relationship to the occurrence of the two cloud heads discussed in section 2. Although there is some subjectivity in identifying the precise duration of the cloud heads, the evidence in Table 1 suggests a link between the coupling of TD1 with the cyclone and the development of cloud head CH1, and similarly between TD2 and CH2. In other words CH1 developed just after TD1 started to deviate toward the cyclone and, similarly, CH2 developed just after TD2 started to deviate toward the cyclone. The period of cyclone deepening appears to overlap the two coupling events. There may have been two separate cyclone centers during the period when two cloud heads coexisted but neither the model nor the sparse in situ observations over the ocean was able to resolve them.

It is probably significant that the cyclone underwent a large and abrupt change in movement (its speed was almost halved for a while and it turned more than 30° to the right) between 28/00 and 28/06 as CH1 gave way to CH2. This occurred just after TD2 had begun to couple with the cyclone. The coincidence in timing leads us to speculate that the discontinuity in movement was somehow related to TD2 superceding TD1 as the dominant upper-level influence. Normally, a cyclone's motion deviates to the left as it deepens. The fact that the opposite happened in this case might have been due to TD2 triggering the development of a separate (unresolved) cyclone center just to the southwest of the existing center and, like TD2, traveling with more of a north-to-south component.

We further speculate that there may have been some direct or indirect coupling between TD1 and TD2. There are two steps in the argument. First we suggest that the coupling of TD1 with the cyclone was responsible for the initial reintensification of the cyclone. This is supported by the fact that TD1 intensified at the same time that the cyclone itself began intensifying (see Table 1). As a result we suggest, secondly, that the intensified cyclone would then have interacted more strongly with TD2 when it subsequently came within range. This is supported by the fact that the track of TD2 began to deviate toward the cyclone when the cyclone was already 6 h into its intensification phase. The authors visualize the interactions metaphorically as follows: TD1 behaves as a picador in triggering the cyclone (the bull) into some initial development; then the strong matador (TD2) comes along and finishes the job, that is, causing the main period of development, not killing it.

4. Errors in NWP model forecasts of the cyclone and the implied analysis errors

a. The errors in the 27/12 forecast run of the operational model

We now examine the forecast for the critical period of intensification and attempt to identify and account for its deficiencies. We limit our consideration to the forecast period out to $T + 24$ and to the run commencing at 27/12. During this period we have reasonable confidence that the analyses were correct on the broadscale (cf. section 5a), whereas at earlier times the forecasts were occasionally bad because they involved interactions between the cyclone and an entirely spurious upper-level feature introduced via the assimilation (Carroll 1997). Within the time range we have chosen, the forecasts, although not good, were at least suggesting interactions with the appropriate tropopause depressions.

Figure 10 shows the location and MSL pressure of the cyclone center between 27/12 and 28/12, as derived from successive 12-h analyses (crosses connected by solid lines) and the corresponding forecasts from the 27/12 forecast run (circles connected by dashed lines). Evidently the forecast position of the low center was 150 km in error by 28/00 and this error doubled in the next 12 h. More significantly, although the forecast did identify some deepening from 27/12 to 28/00, the rate of deepening was too slow by a factor of 4.

A hypothesis to account for the underdevelopment of the cyclone in the 27/12 forecast run is that it was due to the upper-level PV anomaly associated with TD2 being mispositioned. An alternative hypothesis is that the surface cyclone was positioned too far east in the model for interaction to occur; however, we do not have any ground truth to support or quantify this possibility and so we limit our study to a consideration of the positional error in TD2. The mispositioning of TD2 is evident from a comparison between the $T + 12$ forecast (Fig. 11a) and the corresponding analysis for 28/00 (Fig. 11b). The leading part of TD1, with a 300-hPa PV of 4.5 PV units, is close to 51°N, 20°W in both analysis and forecast. The main difference is in the position of TD2, which in the forecast is centered 250 km farther away from the cyclone (X). Subsequently in this forecast run, TD2 was left behind as the cyclone continued traveling to the northeast, and no interaction took place.

TABLE 1. Summary of cyclone evolution during interaction with the two mesoscale tropopause depressions.

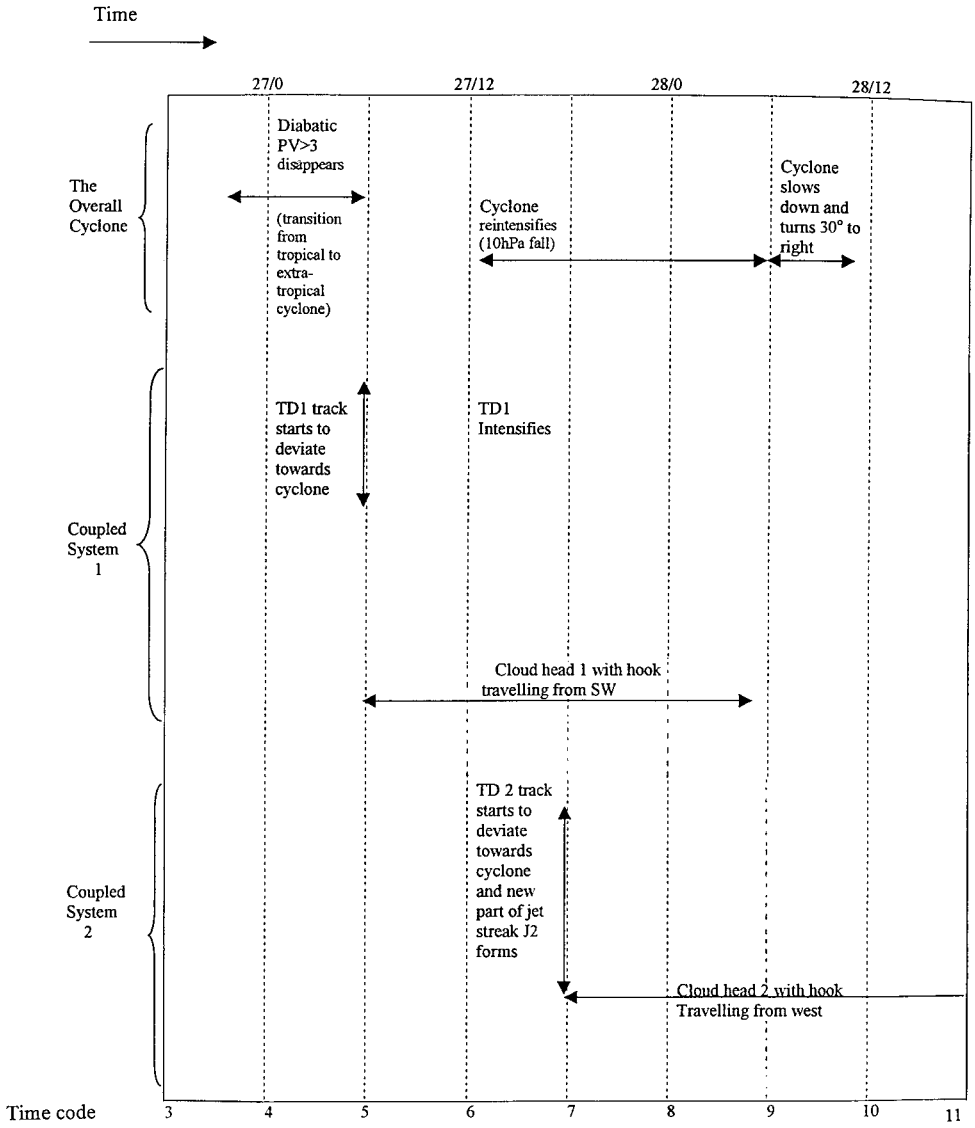

b. Use of known forecast errors to infer the analysis errors

Up to this point all of the model data used in this paper have been from the Unified Model Limited Area Model (LAM). However, we shall now use results from a study using the T-69 version of the ECMWF model, in which singular-vector (SV) analysis has been applied to cyclone Lili (see Montani 1998 for further details). The analysis from the ECMWF model differed greatly from those from the LAM before 27/12 (possibly because of different treatment of a bad observation at 26/12), but for the initial period of cyclone development from 27/12 to 28/00 the two models agreed more closely in their analyses: the central pressure of the surface low agreed to within 2 hPa albeit with a positional error still as large as 200 km at 27/12. We shall now use results obtained from the 27/12 ECMWF forecast run to infer the analysis errors at 27/12 that would account for the observed (i.e., deduced after the event) forecast errors at 28/12.

We use localized singular-vector computations as described in Buizza and Montani (1999). With this method it is possible to find the location of the region, say 24, 36, or 48 h before the valid time of a forecast, where any analysis error would have grown rapidly to reduce the skill of the forecast over a selected target zone. This

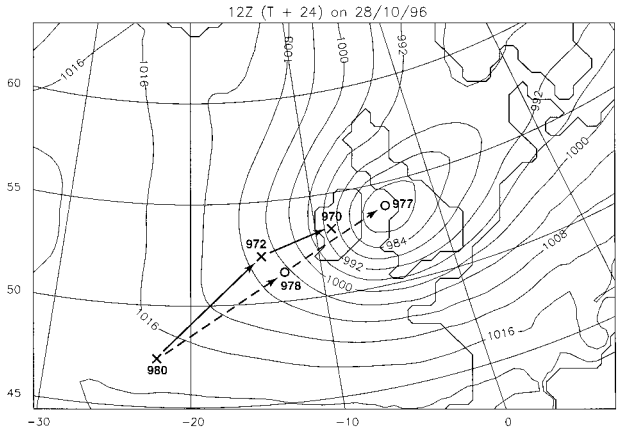

FIG. 10. Comparison of analyzed and forecast tracks of cyclone MSL pressure center superimposed on the 24-h forecast pattern of MSL pressure for 1200 UTC 28 Oct 1996, as derived from the operational run of the Limited Area Model. Solid lines and crosses with MSL pressure labeled in hPa are from analyses at 12-h intervals from 1200 UTC 27 Oct to 1200 UTC 28 Oct 1996. Dashed lines and circles, with MSL pressure labeled, are from the forecast run made at 1200 UTC 27 Oct.

region is referred to as the sensitive region. To make this computation in the case of Cyclone Lili, a target zone was defined (45°–60°N and 10°W–5°E) containing the cyclone at 28/12 (the ''final time''). The SVs were then computed for a number of different ''initial times'' but we restrict the discussion here to those computed 24 h earlier, at 27/12.

We shall discuss later, in section 5b, the horizontal and vertical structure of the first singular vector as a way of identifying the sensitive region in real time. In this section we shall instead invoke the pseudoinverse technique (Buizza et al. 1997) as a means of estimating the analysis errors *knowing the forecast error*. First, in this method the most rapidly growing SVs were calculated from the forecast from 27/12 verifying at 28/12. These SVs maximize the growth of total energy over this time period over the region of the cyclone at 28/12. The forecast error was then projected on the SVs and these projections were used at analysis time to estimate the analysis errors. This method reconstructs the analysis error from the known forecast error if the majority of the forecast error is due to the (linear) growth of the most rapidly growing SVs. The estimate of analysis error improves as more of the complete set of SVs are used. In this case the first 10 SVs were used in an attempt to capture the most significant structures within the forecast error while minimizing computational cost. A total of 24% of the forecast error is explained by these 10 SVs in this case. The analysis error is estimated in terms of local fields of model variables, such as geopotential height, vorticity, and divergence. The analysis is altered by subtracting these error fields from the original analysis. In terms of adjustments to the geopotential height, a 1.6-dam intensification of the 500-hPa trough is implied in the changed region. This is a small but

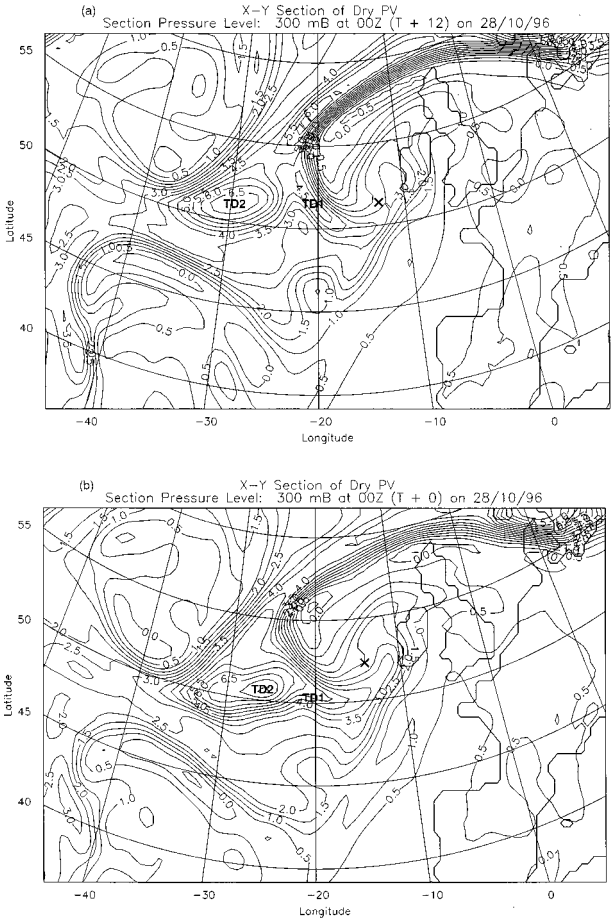

FIG. 11. Comparison between the fields of potential vorticity at 300 hPa as obtained from (a) the operational 12-h forecast verifying at 0000 UTC 28 Oct 1996 and (b) the analysis for 0000 UTC 28 Oct, from the Limited Area Model. Both (a) and (b) show potential vorticity isopleths at intervals of 0.5 PV units. Mesoscale tropopause depressions TD1 and TD2 are labeled. The X shows the model's (a) forecast and (b) analyzed position of the surface cyclone center.

observable error. For comparison with other parts of this paper we also calculate the PV implied by these error fields, simply using the definition of PV in terms of more basic variables. This allowed us to diagnose the PV adjustment needed at analysis time to improve the forecast. The resulting PV adjustment field at 400 hPa is represented in Fig. 12 by the thin contours, the maximum of which can be seen to be centered 600 km south of the 400-hPa PV maximum corresponding to TD2 (and 700 km west of the much weaker TD1). The sign of the adjustment is such as to imply a slight (up to 0.5 PV units) enhancement on the southern flank of TD2 in the modified rerun.

Confirmation of the improvement in the 24-h forecast achieved using the above adjustment is given in Fig. 13. This shows that the error in the forecast mean sea level pressure of the cyclone center decreases from 7 hPa in the operational run (Fig. 13a) to 2 hPa in the modified rerun (Fig. 13b) when compared with the

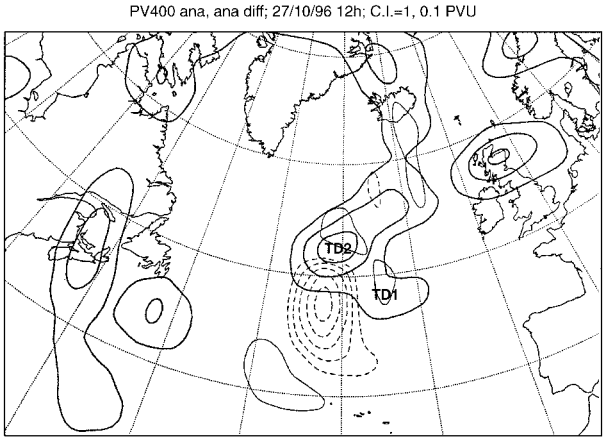

FIG. 12. Estimate of the ECMWF analysis error in potential vorticity valid at 1200 UTC 27 Oct 1996 (thin contours at intervals of 0.1 PV unit, the dashed contours indicating the need for a positive adjustment) superimposed on the unmodified operational ECMWF analysis of potential vorticity at 400 hPa (thick solid contours at intervals of 1 PV unit).

ECMWF analysis in Fig. 13c (which was itself 4 hPa greater than the corresponding LAM analysis). In addition, the analyzed location and shape of the storm, for example, the strong pressure gradient south and west of the cyclone (Fig. 13c), are represented better in the modified run (Fig. 13b) compared with the operational run (Fig. 13a).

In view of the improvement in the 24-h forecast of MSL pressure achieved by applying the adjustment in Fig. 12, it is worthwhile also to consider the associated changes in positions and intensities of the upper-level PV maxima. Figure 14 shows the 300-hPa PV distribution at 28/12 from (panel a) the operational 27/12 forecast run and (panel b) the 27/12 forecast run made using the modified analysis. Comparison with the analyses in Fig. 14c shows that the modified forecast brings the PV maximum somewhat farther east and 200 km closer to the cyclone center (which is itself brought farther west). However, the modified forecast still greatly underestimates the forward advance and intensification of the PV maximum shown in Fig. 14c.

The pseudoinverse method provides only an approximate estimate of analysis error. This is partly because only a limited number of SVs are used. Also the growth of the SVs is linear and dry, whereas growth of perturbations in the full forecast model is, of course, nonlinear with full model physics. Therefore it is not surprising that the forecast reruns are still not perfect. With the first 10 singular vectors we expect to explain at most 29% of the forecast error and so this is probably an upper bound on how much of the analysis error we can find. In fact we find that, in the 24-h ECMWF forecast verifying at 28/12, the rms error in the 1000-hPa geopotential height field decreases from 20.0 m in the operational run to 16.5 m in the perturbed run. The corresponding decrease in rms error at 500 hPa was from

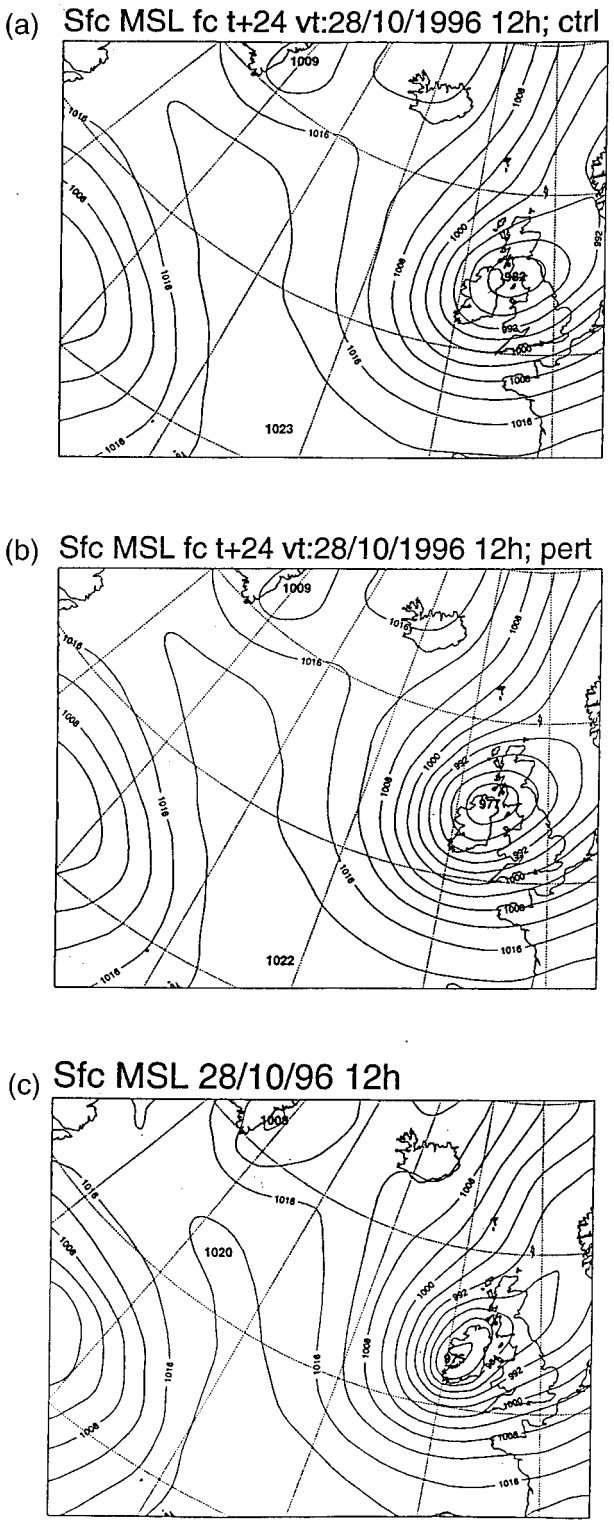

FIG. 13. Comparison between the MSL pressure patterns as obtained from (a) the operational 24-h forecast verifying at 1200 UTC 28 Oct 1996, (b) the modified 24-h forecast for the same time, and (c) the analysis for 1200 UTC 28 Oct, all from the ECMWF model.

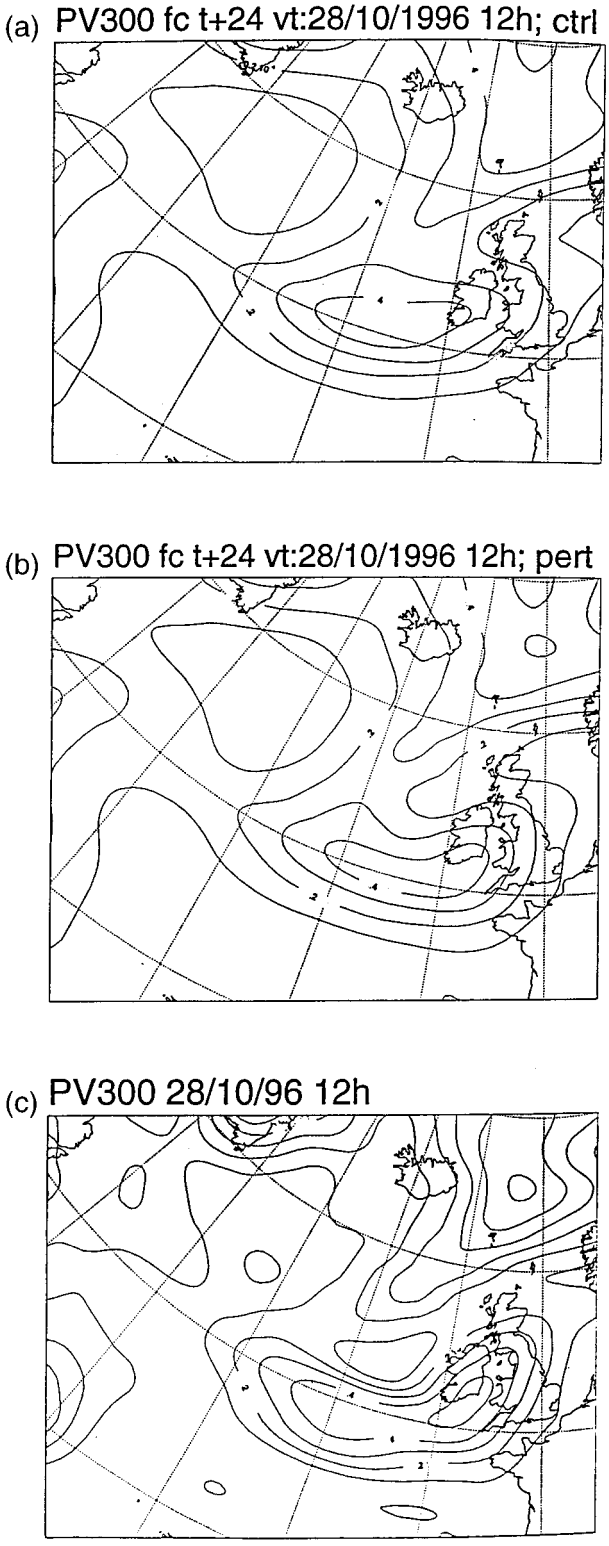

FIG. 14. Similar comparisons as in Fig. 13 but for the fields of potential vorticity at 300 hPa. Potential vorticity contours are at intervals of 1 PV unit.

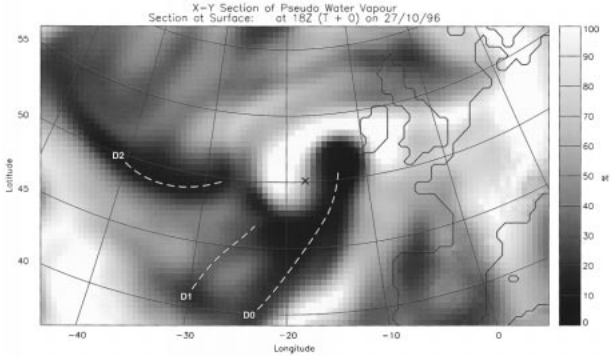

FIG. 15. Pseudo–water vapor image derived as explained in the text from the Limited Area Model analysis for 1800 UTC 27 Oct 1996. The dashed lines draw attention to the axes of the three dark zones corresponding to the upper parts of dry intrusions D0, D1, and D2. The X marks the location of the surface cyclone center.

27.2 to 16.0 m. This translates to an overall improvement of 18% at 1000 hPa and, surprisingly, as much as 41% at 500 hPa. This suggests that the pseudoinverse technique has indeed found part of the actual analysis error.

5. The possibility of assessing analysis errors from information available at analysis time only

a. Identification of errors in the model analyses using water vapor imagery

Information from satellite WV imagery relating to the pattern of upper-tropospheric humidity was not used in the operational NWP model analyses and can therefore be used as an independent check on the analyses. In order to evaluate the model analyses against the satellite imagery we have generated a sequence of pseudo-WV images from successive model analyses. Codes exist that calculate in detail the WV channel radiance that would be expected from the model-derived distribution of moisture and cloud (e.g., Schmetz and van de Berg 1994). For the purpose of this study, however, we have adopted the simple expedient of deriving pseudo-WV imagery by averaging the model's relative humidity at 300, 400, 500, and 600 hPa, and comparing the resulting patterns with the real imagery as in Browning and Roberts (1994b). One of the resulting images is reproduced in Fig. 15.

The pseudo-WV image in Fig. 15 corresponds (within 30 min) to the actual WV image in Fig. 5a. The differences between these two images are partly attributable to the choice of gray scales. However, the most obvious discrepancy is in the extent of the moist (white) area far to the north of the cyclone center (shown as a cross) and we suspect that the model's underestimate of its extent is largely due to the inability of our simple pseudo-WV algorithm to represent the effect of a layer of cirrus cloud at the 300-hPa level. The model also fails to represent the hook of moisture just to the north-

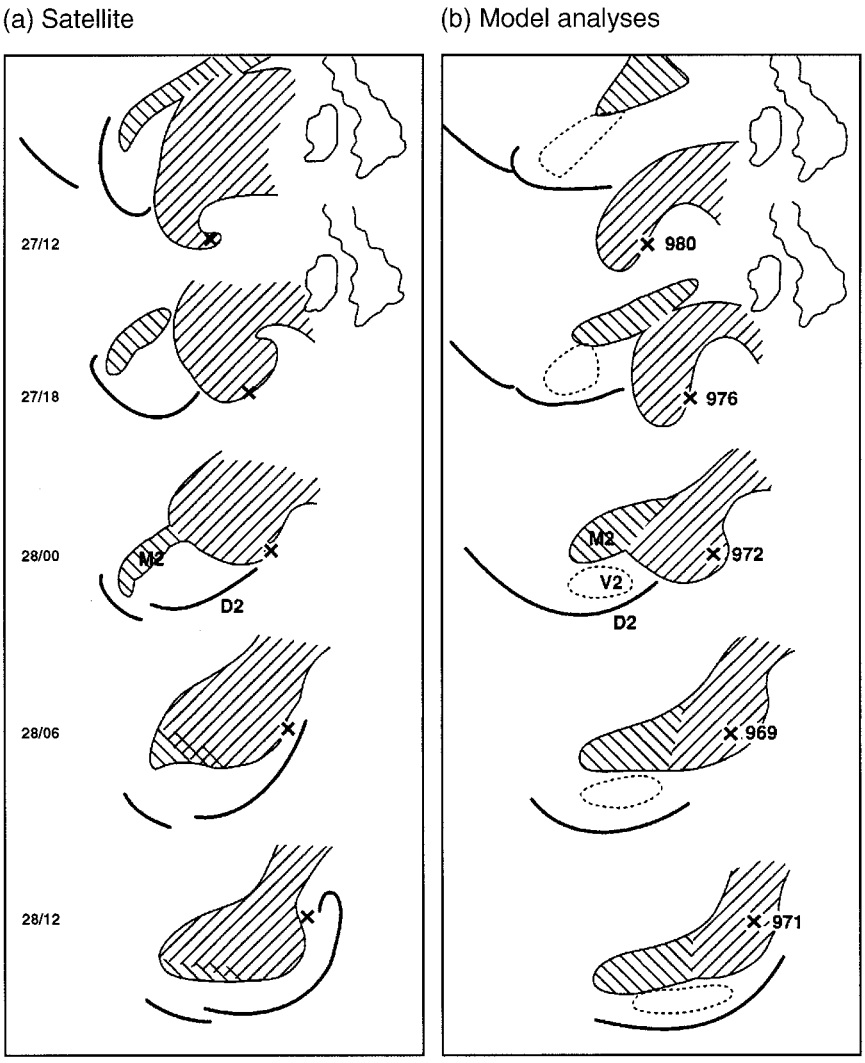

FIG. 16. Sequence of 6-hourly tracings from 1200 UTC 27 Oct until 1200 UTC 28 Oct 1996, showing salient features pertaining to the interaction between the cyclone and the mesoscale tropopause depression TD2, as derived from (a) Meteosat water vapor imagery and (b) Limited Area Model analyses. To prevent overlap, each tracing has been displaced by a constant offset from the previous one, as shown by the positions of the British Isles for the first two times. The north–south extent of the British Isles is about 900 km. The hatched areas show the moist parts of the upper troposphere as given in (a) by brightness temperature below 237 K in the water vapor channel and in (b) by an average relative humidity with respect to ice of 62.5% between 600 and 300 hPa. The main moist area is associated with the cyclone's main cloud head; the smaller moist area to the west (labeled M2), with hatching orientated at right angles to the rest, is associated with TD2. The bold lines in both (a) and (b) represent the axis of the dark zone corresponding to the upper parts of dry intrusion 2 (labeled D2). The dotted contour in (b) represents the core of the upper-level vortex associated with TD2 as given by potential vorticity = 3 PV units at 400 hPa. The mesoscale tropopause depression TD2 became cut off at 300 hPa from the northern trough at 1800 UTC 27 Oct, after which the associated vortex, V2, can be seen to maintain a well-defined spatial relationship to D2 and M2 on either side of it. The model-derived cyclone center is denoted by X and the MSL pressure is labeled in hPa, showing that the main period of deepening was between 1200 UTC 27 Oct and 0600 UTC 28 Oct.

east of the cyclone center. The position of the main cloud-head feature is about right, however. Also, the dark zones associated with dry intrusions D0, D1, and D2 are evident in both Figs. 15 and 5a, where the axes of the dark zones are highlighted by lines passing through the darkest (driest) parts of the images. For the purpose of making detailed intercomparisons at various times, instead of reproducing more pseudo-WV images, we show in Fig. 16 a sequence of tracings of the axis of one of the dry intrusions (D2) derived from the satellite (panel a) and model analyses (panel b). Also shown in Figs. 16a and 16b, respectively, are outlines of the moist/cloud head(s) derived from the WV imagery (shaded for brightness temperature less than 237 K) and from the model (shaded for mean relative humidity from 300 to 600 hPa more than 62.5%).

Agreement between the WV imagery and pseudo-WV imagery in Fig. 16 is qualitatively quite good. Both

show the dry intrusion D2 and an associated moist feature M2 (diagonally hatched in Fig. 16) progressing cyclonically around the western and then southern flank of the main cloud head (diagonally hatched but with different orientation for the hatching). Features D2 and M2 themselves are situated on opposite sides of the maximum in PV (dotted area labeled V2 in Fig. 16b) associated with tropopause depression TD2. As noted above, the shape of the model's main cloud head differs in detail from that in the satellite imagery but its position is in reasonable agreement, being on average perhaps 150 km too far south. The error in the model's dry intrusion D2 is more variable: it is 200 km too far north at the early times, but the error then diminishes to near zero at the later times in Fig. 16. Similar agreement was found for dry intrusion D1 (not shown), although D1 was less well defined and the assessment more difficult to make. The broad overall agreement, in particular the fact that key features in the imagery are recognizable in the model, gives us some confidence in the detailed model diagnoses in sections 2 and 3. However, the positional discrepancies are not negligible, especially at the earlier times. We now tie down these errors a little more precisely by comparing not only the dry part (D2) [as advocated by Mansfield (1997)] but also the moist part (M2) of the vortex (V2) associated with TD2. In referring to the vortex V2 we are using shorthand for the high-PV anomaly in TD2.

The moist feature M2 in Fig. 16, which we shall refer to as a moist head [by analogy with a similar feature analyzed by Browning and Roberts (1994b)], was part of the same vortex V2 that was also responsible for D2. Features M2 and D2 reflect the ascending and descending parts, respectively, of the circulation associated with V2. The interface between them corresponds to the axis of maximum PV, a cross-sectional view of which was shown earlier in Fig. 7a. As can be seen from Fig. 16b, M2 and D2 rotate as a couplet around V2 as V2 itself skirts around the main cloud head. Comparison of Figs. 16a and 16b shows that the model's error in locating M2 displays a similar trend with time to that for dry intrusion D2, albeit with slightly larger errors. We shall take the error in the midpoint of the combined M2–D2 couplet as the best available guide to the model's error in locating the vortex V2. This leads to the result that the model's error in the distance between V2 and the cloud head associated with the main cyclone is 300–400 km toward the north at 27/12 and 27/18. Since the model's cloud head may itself be a little too far north, for the purpose of the analysis that follows we shall assume an error of 300 km at these times. This error decreases in later analyses to less than 150 km, which is close to the error in the assessment.

The adjustment to the analysis suggested by the WV–PV technique is summarized in Fig. 17. The arrow in this figure shows the required 300-km displacement of TD2 superimposed on the operational (unmodified) 27/12 analysis. The apparent inconsistency between the

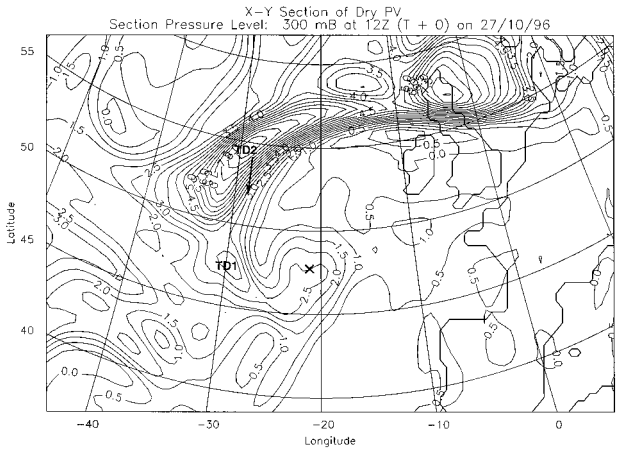

FIG. 17. Field of potential vorticity at 300 hPa as obtained from the operational Limited Area Model analysis at 1200 UTC 27 Oct 1996. Isopleths at intervals of 0.5 PV units plus one at 0.75: mesoscale tropopause depressions TD1 and TD2 are labeled. The arrow denotes the displacement needing to be applied to TD2 to correct the error identified by comparison with WV imagery. The X shows the analyzed position of the surface cyclone center.

north–south error identified here and the west–east error in TD2 identified in Fig. 11 can be reconciled by referring to Fig. 9. The analyzed track of TD2 in Fig. 9a shows that TD2 was traveling southward at 27/12 (time code 6); it then interacted with the cyclone and by 28/00 (time code 8) it was traveling in a more nearly easterly direction around the southern flank of the cyclone. The initial error corresponded to TD2 lagging behind its true position (i.e., it was too far away from the cyclone). The tendency to lag continued but the initial northerly error in TD2 tended to become more of a westerly error, with TD2 still too far away from the cyclone.

b. Use of singular vectors to point to the sensitive region

We have already presented, in section 4b, the results of pseudoinverse calculations based upon the singular-vector analysis. This was done in order to estimate the analysis error given a knowledge of the error in the forecast. We now present the basic results of the singular-vector calculations that would be available at or prior to the analysis time. These singular vectors are the structures that grow the most rapidly over the period 27/12 to 28/12 to have maximum amplitude in the region of the cyclone at 28/12. At the initial time, 27/12, the location of the singular vectors indicates the region where, if there were an analysis error, it would grow significantly during the forecast. As noted earlier these are called sensitive regions. These are the regions where the forecasts could be expected to benefit from additional targeted observations. The vertical profile of total energy for the first SV (Fig. 18) shows that the most sensitive region at 27/12 was at approximately 400 to

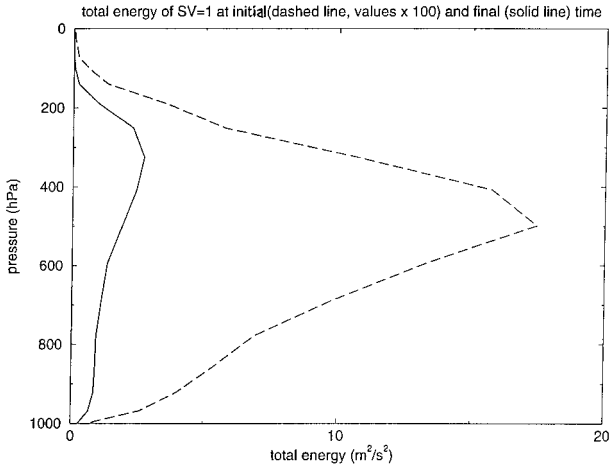

FIG. 18. Vertical profile of total energy (in $m^2\ s^{-2}$) at the initial time, 1200 UTC 27 Oct 1996 (dashed line, values multiplied by 100) and at the final time, 1200 UTC 28 October (solid line) for the first 24-h singular vector, based upon the ECMWF model.

500 hPa, that is, close to the level of the depressed tropopause. The high sensitivity found at this level helps to justify our preoccupation with the role of tropopause disturbances, which is the underlying theme of this paper. It is, however, in contrast to the results of sensitivity studies for most other cases, which tend to show greatest sensitivity in the lower troposphere (e.g., Montani 1998).

Figure 19 shows the horizontal structure of the first singular vector (i.e., the fastest growing singular vector) at 27/12 at 325 hPa and 400 hPa, superimposed on the basic state of PV. The structure of the SV exhibits a series of positive and negative perturbations, like a wave train, elongated in the southwest to northeast direction. Figure 12, obtained with the benefit of hindsight, suggested that the maximum analysis error at this time was at 48°N, 32°W. From Fig. 19 we see that this is within the region indicated by the first singular vector and is just to the south of the position of TD2 adjusted as indicated by the arrow in Fig. 17. In other words, the WV–PV and SV methods, although by no means in perfect agreement, do point to the same broad area in which the analysis required adjustment. Bearing in mind that this agreement is based upon two independent operational models (the ECMWF model and the Met Office Unified Model), this is quite encouraging.

In the next section we apply an adjustment to the initial PV field (derived from the WV–PV method rather than the SV method) to see if it improves the forecast evolution. We do this using the Unified Model and for consistency we apply the 300-km displacement determined for that model in section 5a.

6. Effect of PV modification on the forecast

The general hypothesis that a model forecast can be improved by modifying the PV field in accordance with

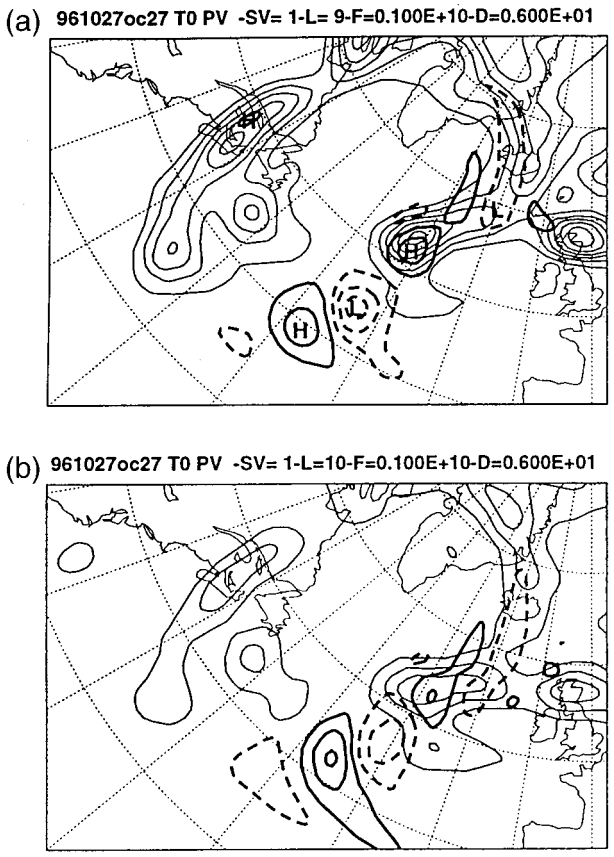

FIG. 19. Sensitive regions (in PV) inferred from the first singular vector in the ECMWF model, superimposed on the basic-state analysis of PV, for 1200 UTC 27 Oct 1996 at (a) 325 and (b) 400 hPa. Thick contours indicate the PV structure (solid, positive; dashed, negative) of the singular vector. Note that the amplitude is arbitrary. Thin contours indicate basic-state PV, with a contour interval of 1 PV unit.

errors in the initialization follows from the work of Mansfield (1997), Carroll (1997), and Demirtas and Thorpe (1999). We employ the PV inversion method described in Griffiths et al. (1999), which is similar to that used by Demirtas and Thorpe (1999) and Fehlmann and Davies (1997). First we change the PV field over a limited area and then we use PV inversion to obtain new estimates of the wind and temperature fields from the modified PV field. The assumption for the inversion is the nonlinear balance described in Davis and Emanuel (1991), with a lower boundary condition of the theta field being unaltered by the PV modifications. A difference between our work and that of Demirtas and Thorpe (1999) is that we did not employ data assimilation and treat these modifications as bogus observations; rather we directly modified the analysis. This new analysis was used to initialize the Limited Area Model for a 24-h forecast starting at 27/12.

The PV has been modified in the Unified Model analysis at 27/12 by displacing TD2 approximately 300 km toward the south between 500 and 250 hPa. The basis

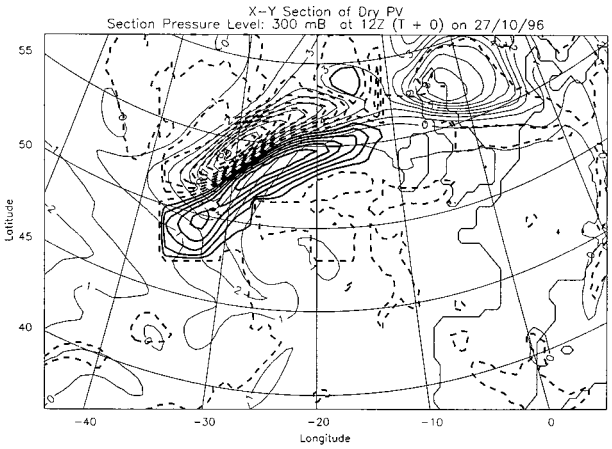

FIG. 20. Estimate of the analysis error in potential vorticity valid at 1200 UTC 27 Oct 1996 (thick contours at intervals of 1 PV unit; solid, positive and dashed, negative) superimposed on the unmodified operational Limited Area Model analysis of potential vorticity at 300 hPa (thin solid contour at intervals of 1 PV unit). The operational analysis shown here differs slightly from that shown in Fig. 17 for reasons that are explained in the text.

for a displacement of this magnitude was presented in section 5a. The PV modification actually applied, to correspond to such a displacement, is shown in Fig. 20 together with the operational PV field at 300 hPa. Although the overall sense of the modifications applied, both in the Unified Model (Fig. 20) and previously in the ECMWF model (Fig. 12), is such as to increase the magnitude of the PV to the south of TD2, an examination of the detailed modifications in these two figures shows that the changes are quantitatively quite different, with the largest increment in the PV field in Fig. 20 occurring more to the southeast of the center of TD2.

The PV fields at 300 hPa calculated for the 24-h forecasts without (FOP) and with (FMOD) the southward displacement of TD2 are shown in Figs. 21a and 21b, respectively. The corresponding analysis is shown in Fig. 21c, at which time TD1 and TD2 had peak intensities of over 6 and 7 PV units, respectively. Although the peak value of TD2 is somewhat too low in FMOD (Fig. 21b), its location is seen to be much closer to its analyzed position (Fig. 21c) than it is in FOP (Fig. 21a). The displacement of TD2 closer to the cyclone suggests that it is in a better position to interact with it. The representation of TD1, however, is significantly worse in FMOD (Fig. 21b) than in FOP (Fig. 21a). These opposing influences may be part of the reason why the resulting improvement in the MSL pressure field (not shown) was negligible. The forecast of the central pressure for the modified forecast (FMOD) was essentially the same as the forecast of 977 hPa for the unmodified operational forecast (FOP).

A practical computing problem we encountered may be part of the reason for the disappointing lack of improvement. Corruption of a data tape during the course of the research forced us to regenerate the operational

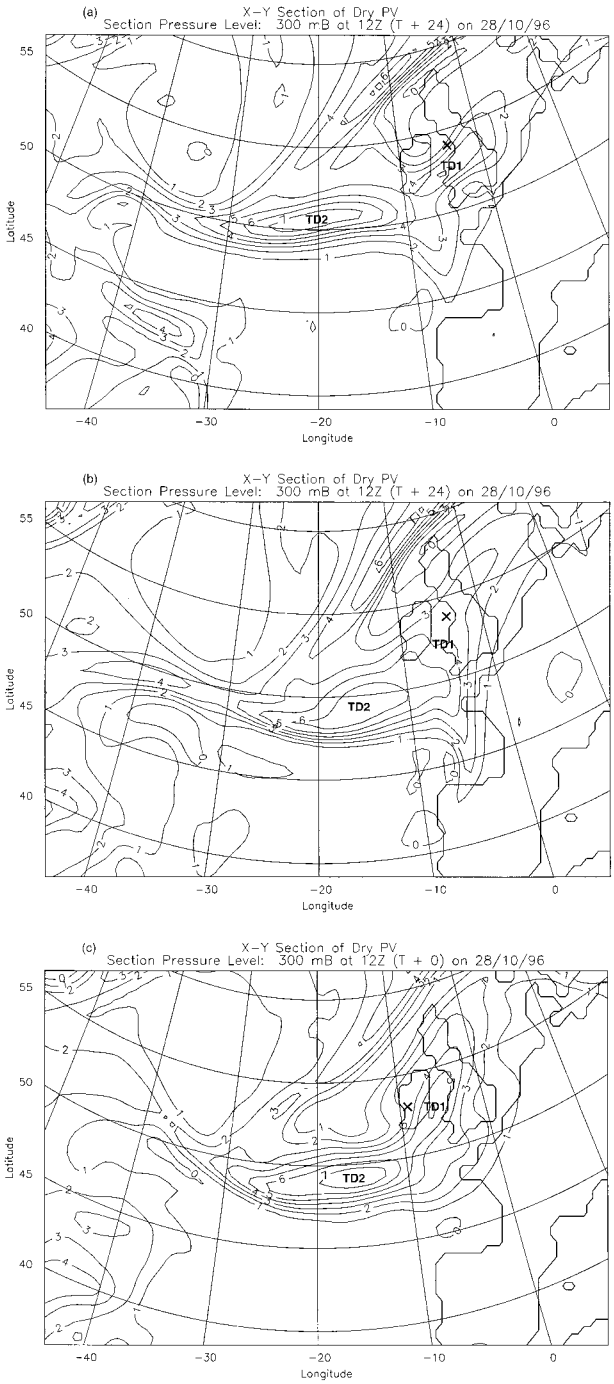

FIG. 21. Comparison between the fields of potential vorticity at 300 hPa as obtained from (a) the operational 24-h forecast (FOP) verifying at 1200 UTC 28 Oct 1996, (b) the modified 24-h forecast (FMOD) for the same time, and (c) the analysis for 1200 UTC 28 Oct, all from the Limited Area Model. See text in section 6 for explanation of the modification underlying (b). Potential vorticity isopleths are at intervals of 1 PV unit: mesoscale tropopause depressions TD1 and TD2 are labeled. The X shows the surface cyclone center.

analysis from the global fields but without access to the additional observational input. As a result, the so-called operational analysis shown by the thin contours in Fig. 20, while very similar to the genuine operational analysis shown in Fig. 17 (and producing a rather similar 24-h forecast), does nevertheless exhibit some small differences. There is, in particular, a significant difference in the magnitude of the 300-hPa PV in the vicinity of TD1, which has a peak value of over 3.5 units in Fig. 17 compared with about 2.5 units in the regenerated operational analysis in Fig. 20. This might account for the deterioration in the representation of TD1 in the forecast run, FMOD, in Fig. 21b, which in turn may have had a significant impact on the predicted cyclogenesis. There is, however, another possible reason for the lack of improvement in the modified forecast, which we explain next.

The method we have used to modify the analysis inserts only the nondivergent component of the wind in the modification region. It is thought that the associated divergent flow will develop in the initial stages of the forecast. If the forecast is over a relatively long period such as 48 or 60 h, then this initial adjustment may not be important; however, this is less evidently so for a 24-h forecast such as is carried out here. It might be possible to estimate the divergent wind from the PV inversion but this is not done here as it remains unclear how to do this consistently for the level of approximation used in the PV inversion. Instead we have created an alternative control (FAC) wherein the unmodified PV is inverted and the forecast rerun, minus the divergent winds in the proposed modification region. The result of the FAC (not shown) was to degrade prediction of the low pressure center from 977 to 979 hPa at 24 h. We draw two conclusions from this result. First, it is evident that the modification of the PV field has a greater positive impact than one would initially suspect from comparison against the FOP alone. In this context the relative deepening achieved by moving TD2 appears to have been about 2 hPa. The error in the FAC forecast with unmodified PV was about 9 hPa.

The more general implication of this result is that there is potentially a detrimental effect in the inversion process arising from ignoring the divergent component of the wind field. Simply recalculating the PV from the inverted quantities, as proposed by Fehlmann and Davies (1997), will not detect this type of shortcoming. The inclusion of the divergent component of the winds is possible within our formulation and this should be explored in the future. Comparisons between the operational forecast and the two simulations where PV inversion was used to derive the initial conditions show a pronounced reduction (which increased with time) in the low-level PV fields for the inverted simulations. Since this low-level PV feature was collocated with upward motions and the rainfall field, we suspect that this change is associated with the neglect of the divergent component.

Although we did obtain some deepening in the simulation with the modified PV (FMOD) relative to a proper control experiment (FAC), the magnitude of the improvement is still disappointing. To test whether this behavior was due to errors in our estimation of the PV displacement, we conducted a series of separate sensitivity tests where the angle of displacement was varied from southerly to SSW and SSE and also where the displacement distance was halved (from 300 to 150 km). The magnitude of the central low pressure varied by only about 1 hPa in these different experiments, suggesting that any modest errors in our estimation of the displacement of TD2 did not account for the lack of pronounced deepening in these forecasts.

The relatively weak impact of modifying the PV distribution of the analysis is an important issue needing to be addressed further. Consideration of PV as a conserved quantity might lead one to suggest including very localized adjustments in the expectation that such adjustments would retain a spatial coherence. In fact there is a wave dispersion component that might tend to discourage one from making such localized modifications. Other factors that might explain the limited impact of modifying the PV distribution include (i) the possibly adverse effect of neglecting the divergent wind in the present PV inversion process; (ii) the impact of unmodified lateral boundary conditions for the Unified Model simulations and errors in the large-scale setting for the ECMWF model; (iii) finite model resolution, as past work indicates that there is often a dependence of the prediction of the central low pressure on the horizontal grid spacing; (iv) other errors in the three-dimensional depiction of the PV in the analysis, particularly in the lower and middle levels where PV is created by diabatic processes; and (v) shortcomings in the model physics. In our case, the Unified Model and ECMWF model reruns both failed to improve the positioning of the low center. The formation of a second cloud head and deepening of the low near Ireland as the mesoscale tropopause depression TD2 approached suggest a type of secondary development that the models were unable to replicate. A valuable discussion of model errors for a case of secondary development off the coast of North America can be found in Gyakum et al. (1995).

7. Conclusions

Many strands of evidence have been brought together in this study, both from observations (Meteosat) and from NWP models (the LAM version of the U.K. Meteorological Office Unified Model and the T-69 version of the ECMWF model). The findings and their interdependence may be summarized as follows.

1) The reintensification of Tropical Cyclone Lili shortly after becoming an extratropical cyclone was plausibly associated with its interaction with two mesoscale tropopause depressions, TD1 and TD2, that

approached it after becoming cutoff from different troughs to the west and north of the cyclone, respectively.
2) Each of these mesoscale tropopause depressions generated its own cloud head and each is believed to have contributed to the deepening of the surface cyclone.
3) Each mesoscale tropopause depression had a characteristic 3D structure as seen in the Unified Model, with dry-intrusion air descending slantwise beneath its own upper-level jet streak.
4) The mesoscale tropopause depressions could be identified from the patterns of upper-level moisture seen in the Meteosat water vapor imagery. The second mesoscale tropopause depression, TD2, in particular, had a well-defined vortex-related WV signature that consisted of not only a ''dark zone'' due to dry, upper-level air descending on the right hand side of the vortex, but also a corresponding ''gray zone,'' or ''moist head,'' due to moist air ascending at upper levels on the left-hand side of the vortex. The WV signature has been used to identify errors in the model analyses of one of the mesoscale tropopause depressions.
5) Both mesoscale tropopause depressions could be tracked at 300 hPa during a long series of model analyses as they approached and then coupled with the cyclone. The coupling was evident from a rather abrupt change in their propagation velocity once they came within the radius of influence of the cyclone's warm core. After coupling, the two mesoscale tropopause depressions followed similar tracks around the right (southern) flank of the cyclone.
6) The second and larger of the two mesoscale tropopause depressions, TD2, failed to couple in the 27/12 operational forecast run of the Unified Model. The 300-km error in the position of TD2 (identified as in point 4 above) was in the right sense (i.e., too far away from the cyclone) to account for its failure to couple.
7) The deepening of the cyclone was significantly underestimated in the 27/12 forecast run and it is hypothesized that this was due to the estimated 300-km error in the analyzed position of mesoscale tropopause depression TD2. This hypothesis was tested by adjusting the position of the local maximum in the PV distribution associated with TD2 using the technique of PV surgery. This achieved a perceptible improvement in the forecast track of TD2. However the improvement in msl pressure was negligible.
8) The inference that the forecast error was due to a positional error of an upper-level feature in the analysis is supported by a singular-vector analysis using the ECMWF model. The main sensitive region was identified just below 400 hPa and to the south of the main tropopause depression TD2. A corresponding analysis error implying a PV adjustment was identified using a pseudoinverse technique, based on the known forecast error. When this estimated analysis error was removed a more realistic behavior of the tropopause depression and a significantly improved forecast of the deepening of the cyclone occurred, thereby giving confidence in the identification of analysis errors.

The recent findings of Fehlmann and Davies (1997) and Demirtas and Thorpe (1999) indicate that distinct improvements in the model forecasts are possible when modifications are made to the PV field, particularly when the forecast errors are very large. The results of our PV surgery and singular-vector analyses herein also suggest that modification of the upper-level PV fields can improve the model forecast. However, in this study, the impact on the deepening of the low center was small and the error in the position of the low was not greatly improved.

While acknowledging the need to reduce model errors, there is also a clear requirement, especially over data-sparse areas such as the North Atlantic storm track, to improve the analyses from which forecasts are made. We have used two methods in this study to locate analysis errors and to remove or at least reduce them. These methods can be used in real time. The first is the translation of an error identified (via satellite imagery) in the WV field into thermal and kinematic information via PV inversion. Using PV thinking allows both an identification of the existence of an analysis error as well as an estimation of that error. The second method, using SVs, is to calculate so-called sensitive regions where if there is an analysis error, then this error will grow rapidly. In order to reduce such an error, the use of pilotless aircraft to take additional localized observations would be an exciting possibility. In the case studied here the regions highlighted by these two methods were essentially collocated; it remains for further research to establish the generality of this result. In other cases of extratropical cyclones, such as observed in the Fronts and Atlantic Storm-Track Experiment, the sensitivity is more commonly in the lower troposphere rather than near tropopause level as in the present case, although even then there may be a clear dynamical link with nearby structures such as tropopause depressions.

Acknowledgments. The Joint Center for Mesoscale Meteorology is supported by the U.K. Meteorological Office and the Department of Meteorology, University of Reading, Reading, United Kingdom. This research was undertaken under the auspices of the U.K. Universities Weather Research Network funded by the Natural Environment Research Council.

REFERENCES

Bader, M. J., G. S. Forbes, J. R. Grant, R. B. E. Lilley, and A. J. Waters, 1995: *Images in Weather Forecasting.* Cambridge University Press, 499 pp.

Böttger, H., M. Eckardt, and U. Katergiannakis, 1975: Forecasting

extratropical storms with hurricane intensity using satellite information. *J. Appl. Meteor.,* **14,** 1259–1265.
Browning, K. A., 1997: The dry intrusion perspective of extra-tropical cyclone development. *Meteor. Appl.,* **4,** 317–324.
——, and N. M. Roberts, 1994a: Structure of a frontal cyclone. *Quart. J. Roy. Meteor. Soc.,* **120,** 1535–1557.
——, and ——, 1994b: Use of satellite imagery to diagnose events leading to frontal thunderstorms: Part 1 of a case study. *Meteor. Appl.,* **1,** 303–310.
——, S. A. Clough, C. S. A. Davitt, N. M. Roberts, T. D. Hewson, and P. G. W. Healey, 1995: Observations of the mesoscale substructure of the cold air of a developing frontal cyclone. *Quart. J. Roy. Meteor. Soc.,* **121,** 1229–1254.
——, S. P. Ballard, and C. S. A. Davitt, 1997: High resolution analysis of frontal fracture. *Mon. Wea. Rev.,* **125,** 1212–1230.
——, G. Vaughan, and P. Panagi, 1998: Analysis of an ex-tropical cyclone after its reintensification as a warm-core extratropical cyclone. *Quart. J. Roy. Meteor. Soc.,* **124,** 2329–2356.
Buizza, R., and A. Montani, 1999: Targeting observations using singular vectors. *J. Atmos. Sci.,* **56,** 2965–2985.
——, R. Gelaro, F. Molteni, and T. N. Palmer, 1997: The impact of increased resolution on predictability studies with singular vectors. *Quart. J. Roy. Meteor. Soc.,* **123,** 1007–1033.
Carroll, E. B., 1997: Poorly forecast trough disruption shown in water vapor images. *Meteor. Appl.,* **4,** 229–234.
Cullen, M. J. P., 1993: The unified forecast climate model. *Meteor. Mag.,* **122,** 81–94.
Danielsen, E. F., 1964: Project Springfield report. Defense Atomic Support Agency, Washington, DC, 97 pp. [NTIS AD-607980.]
Davies, H. C., and A. M. Rossa, 1998: PV frontogenesis and upper-tropospheric fronts. *Mon. Wea. Rev.,* **126,** 1528–1539.
Davis, C. A., and K. A. Emanuel, 1991: Potential vorticity diagnostics of cyclogenesis. *Mon. Wea. Rev.,* **119,** 1929–1953.
Demirtas, M., and A. J. Thorpe, 1999: Sensitivity of short-range weather forecasts to local potential vorticity modifications. *Mon. Wea. Rev.,* **127,** 922–939.
Fehlmann, R., and H. C. Davies, 1997: Misforecasts of synoptic systems: Diagnosis via PV retrodiction. *Mon. Wea. Rev.,* **125,** 2247–2264.
Griffiths, M., A. J. Thorpe, and K. A. Browning, 2000: Convective destabilisation by a tropopause fold diagnosed using potential vorticity inversion. *Quart. J. Roy. Meteor. Soc.,* **126,** 125–144.
Gyakum, J. R., and Coauthors, 1995: First COMPARE Workshop: 3–5 October 1994, Montreal, Quebec, Canada. *Bull. Amer. Meteor. Soc.,* **76,** 1209–1218.
Hoskins, B. J., M. E. McIntyre, and A. W. Robertson, 1985: On the use and significance of isentropic potential vorticity maps. *Quart. J. Roy. Meteor. Soc.,* **111,** 877–946.
Joly, A., and Coauthors, 1997: The Fronts and Atlantic Storm-Track Experiment (FASTEX): Scientific objectives and experimental design. *Bull. Amer. Meteor. Soc.,* **78,** 1917–1940.
Mansfield, D. A., 1997: The use of potential vorticity and water vapor imagery to validate numerical models. *Meteor. Appl.,* **4,** 305–309.
Montani, A., 1998: Targeted observations for cases of cyclogenesis. Ph.D. thesis, University of Reading, 180 pp. [Available from Main Library, Dept. of Meteorology, University of Reading, White Knights, Reading RG6 6AE, United Kingdom.]
——, A. J. Thorpe, R. Buizza, and P. Under, 1999: Forecast skill of the ECMWF model using targeted observations during FASTEX. *Quart. J. Roy. Meteor. Soc.,* **125,** 3219–3240.
Schmetz, J., and L. van de Berg, 1994: Upper tropospheric humidity observations from Meteosat compared with short-term forecast-fields. *Geophys. Res. Lett.,* **21,** 573–576.
Snyder, C., 1996: Summary of an informal workshop on adaptive observations and FASTEX. *Bull. Amer. Meteor. Soc.,* **77,** 953–961.
Thorpe, A. J., 1997: Attribution and its application to mesoscale structure associated with tropopause folds. *Quart. J. Roy. Meteor. Soc.,* **123,** 2377–2399.
Uccellini, L. W., 1990: Processes contributing to the rapid development of extratropical cyclones. *Extratropical Cyclones: The Erik Palmer Memorial Volume,* C. W. Newton and E. O. Holopainen, Eds., Amer. Meteor. Soc., 81–105.
Weldon, R. B., and S. J. Holmes, 1991: Water vapor imagery, interpretation and applications to weather analysis and forecasting. NOAA Tech. Rep. NESDIS 57, 213 pp. [Available from National Technical Information Service, U.S. Dept. of Commerce, Sills Building, 5285 Port Royal Road, Springfield, VA 22161.]
Young, M. V., G. A. Monk, and K. A. Browning, 1987: Interpretation of satellite imagery of a rapidly deepening cyclone. *Quart. J. Roy. Meteor. Soc.,* **113,** 1089–1115.